Schweizerische Eidgenossenschaft
Confédération suisse
Confederazione Svizzera
Confederaziun svizra

Department of the Environment, Transport, Energy and Communication DETEC

Swiss Federal Office of Energy SFOE
Energy Research

Final report (draft)

Designing multifunctional materials for proton exchange membrane fuel cells

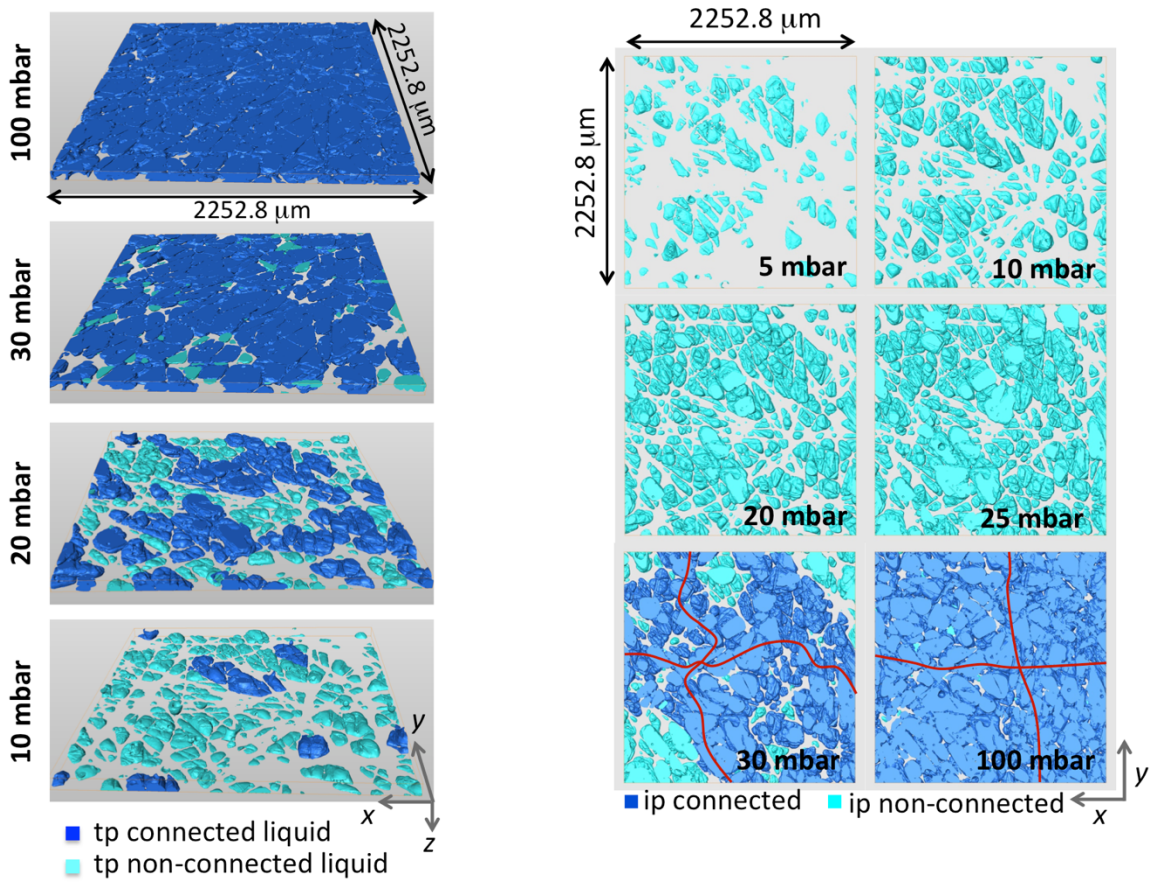

Visualization of the connectivity of liquid water, which is intruding the gas diffusion layer of a proton exchange membrane fuel cell from the bottom layer due to pressure induced injection. The images are acquired by means of X-ray-tomography. Fibres and empty pores are not shown (transparent).

Left: Through-plane. Light blue represents liquid clusters that are not connected with the top layer. Dark blue represents water clusters that are vertically percolating. The through-plane 'pseudo- breakthrough' evolves continuously over an extended pressure range from 5 to >30 mbar.

Right: In-plane. Light blue represents liquid clusters that have no in-plane connectivity. Dark blue represents water clusters that percolating in plane (e.g. from left to right or from top to bottom). The in-plane breakthrough is a discontinuous, abrupt event, that takes place at approx. 27 mbars.

Date: December 2017
Town: Bern

Publisher:
Swiss Federal Office of Energy SFOE
Hydrogen Research Programme
CH-3003 Bern
www.bfe.admin.ch

Co-financed by:
Swiss National Science Foundation SNSF
Wildhainweg 3
CH-3001 Bern
Funding scheme NFP70 Energy Turnaround
SNSF project number 153790
http://p3.snf.ch/project-153790

Agent:
Jürgen Schumacher
Zurich University of Applied Sciences ZHAW
Institute of Computational Physics ICP
Wildbachstrasse 21
CH-8401 Winterthur
http://www.icp.zhaw.ch

Authors:
Jürgen O. Schumacher, Roman Vetter, Luigino Capone, Lorenz Holzer, ZHAW-ICP, schm@zhaw.ch
Adrien Lamibrac, Felix Büchi, PSI, felix.buechi@psi.ch

SFOE head of domain: Rolf Schmitz, rolf.schmitz@bfe.admin.ch
SFOE programme manager: Stefan Oberholzer, stefan.oberholzer@bfe.admin.ch
SFOE contract number: SI/501129-01

Swiss Federal Office of Energy SFOE
Mühlestrasse 4, CH-3063 Ittigen; postal address: CH-3003 Bern
Phone +41 58 462 56 11 · Fax +41 58 463 25 00 · contact@bfe.admin.ch · www.bfe.admin.ch

1. Project goals

This project focuses on the investigation of the relationship between the microstructure and the transport properties in the porous layers (GDL, MPL) of PEFCs. A detailed understanding of these relationships are necessary to develop specialized materials, to attempt an introduction of PEFCs into the market. For this purpose, a multi-scale model is developed to analyze and design PEFCs – the model is based on the material properties that are extracted from the pore scale of the materials by means of tomography and microstructure modelling.

The project objectives are:

- Microstructure and liquid water phase analysis of porous layers of PEFCs
- Development of a software to simulate the coupled transport processes in PEFCs; taking into account the transport of the gas components, liquid water, heat and charge
- Computer aided design of materials for PEFCs
- Contributing to the introduction of PEFCs to the market by raising flow rates in porous materials (gases, charge, heat, and water); improving surfaces to avoid interfacial flow barriers

Transport of gases and liquid water within the gas diffusion layer (GDL) is a critical issue to improve performance and efficiency of proton exchange membrane fuel cells (PEFC). In order to understand how reactants and products of the electrochemical reactions flow through GDLs, a special attention should be given to the GDL microstructure. In particular it is still unclear what geometrical parameters are relevant to describe appropriately liquid water transport.

In order to establish criteria for materials optimization it is necessary to understand how microstructure characteristics influence transport properties (e.g. gas diffusivity, liquid permeability, electrical conductivity) in the various porous layers. For this purpose we perform 3D analysis of the porous materials (MPL, GDL), in order to extract relevant topological parameters of pore, solid and water phases such as tortuosity, constrictivity, connected volume fraction, specific surface/interface areas. The 3D data are obtained either by tomography (micro-CT for GDL, FIB-SEM for MPL) or they can be virtually created (e.g. with Geodict). The effective properties are then obtained by numerical simulation of transport on the voxel grid (e.g. in GeoDict). In this way the effective properties can be correlated with the measured microstructure characteristics (topological parameters) on a quantitative level.

For the GDL there are three particular challenges when studying microstructure-property relationships. First, the fibrous layer undergoes significant deformation when compressed in a cell configuration. Therefore, the microstructure of the GDL needs to be studied as a function of compression level. Second, the fibrous materials are highly anisotropic. Capturing the anisotropy by means of volume averaged parameters is not standardized for all parameters and this issue requires special attention. Third, the effective properties of gas and liquid phases depend on the state of saturation. Here we need to extract the relative property (e.g. relative liquid permeability, relative gas diffusivity), which describe the material behavior at a certain saturation level in relation to the same property at dry state.

From detailed micro-macro-relationship, using the information coming from the imbibed structure and the Monte-Carlo simulation of the water distribution, it will be possible to simulate the effect of water in

real or virtual microstructures using GeoDict. For each of the saturation steps we then determine microstructure characteristics and transport properties in gas, liquid and solid phases.

One objective of the project work was to take into account the previously determined effective porous material properties in a newly developed macrohomogeneous model of a PEFC. Water saturation profiles in the porous layers and the electrochemical production rate of water need to be predicted by the PEFC model. The model shall be used to investigate the influence of the pore- and material surface structure on the water distribution and the PEFCs performance.

2. Summary

Microstructure characterization of both dry and partially saturated gas diffusion layers (GDLs) has been accomplished. X-ray tomographic images under different compression levels allowed for the deduction of porous material properties. **New improved quantitative relationships** between GDL microstructure and effective transport properties have been established. Ex-situ experiments of GDLs imbibed with liquid water were carried out. The dependency of microstructure features on liquid water saturation lead to new insight on finite size effects in thin porous media, delivering valuable input for macro-homogeneous models.

To enhance the understanding of effects governing **liquid water distribution** in the pore space of GDLs, a **3D pore-scale Monte Carlo model** has been developed and validated, which minimizes the surface free energy of the water. Simulation results on the water distribution in real GDL geometries were compared to the experiments.

To develop multifunctional materials for improved PEFC performance, better understanding of the liquid water interface between GDL and gas channels is needed. Fast X-ray tomographic microscopy has been applied to study the **dynamic pressure-saturation relationship and droplet formation and removal** in the vicinity of the interface. An analytical model of the same mechanism has been developed, and the dynamic response of water saturation levels in GDLs to such boundary conditions has been studied.

Macrohomogeneous models of the membrane electrode assembly and of small area PEFCs have been developed. The material parameterizations of these models were revised, and simulated cell performance was compared to measurement data. The combination of microstructure analysis of porous materials and macrohomogeneous fuel cell performance simulation is applied for the **design of multifunctional materials**, that is, to develop new porous transport layers and membrane electrode assemblies. The methodology is interesting for companies in the value added chain of hydrogen fueled electric vehicles, other PEFC powered electric devices but also for electrochemical cells like redox flow cells for the storage of electricity from solar cells or wind mills.

A web page is being created for the **marketing of mathematical models of electrochemical cells**, offering consulting to companies and laboratories, and to disseminate selected project results.

3. Work undertaken and findings obtained

3.1. X-ray tomographic microscopy imaging of gas diffusion layer

GDLs are usually constituted of some micrometer diameter fibers hold together by a binder. A very appropriate technique to investigate this porous material is X-ray tomographic microscopy. The obtained 3D gray-scale images have a resolution of typically around 2 micrometer and fiber, binder as well as void can be resolved. Using post processing imaging, segmentation can be done to differentiate the solid phase (fiber and binder) from the void phase

3.1.1. Dry structure characterization

In a first step, influence of compression on porosity is investigated. A 6 mm diameter SGL 25BA is compressed between two plain flow fields. Six compressions are applied ranging from 11% to 49%. For each compression a scan is performed using a CT scanner nanotoM from General Electrics. The resolution achieved is 3.4 µm per pixel.

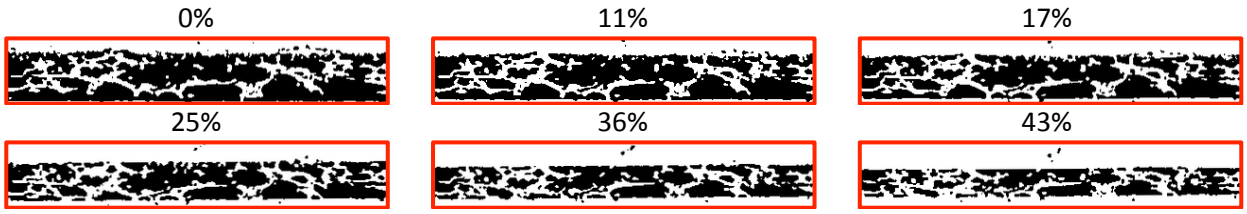

Figure 1: Segmented through-plane slice of a SGL 25BA under different compressions

Quantitative information can be deduced from 3D segmented images such as the local porosity. Figure 2 shows the strong heterogeneity of the porosity across the GDL thickness with higher values at the edges and local minima and maximum in the bulk. This heterogeneity is conserved while the compression is increased. Gas and water transports are expected to be influenced by these spatial variations.

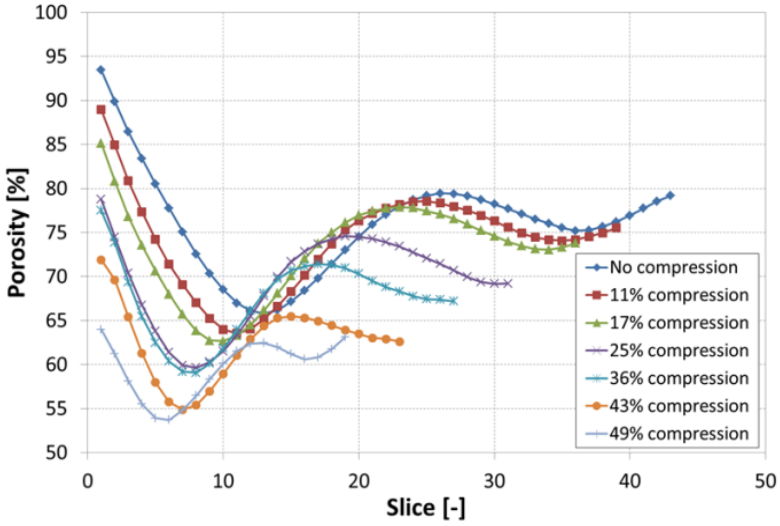

Figure 2: In-plane porosity as a function of the through-plane position for different compressions

3.1.2. Saturated GDL

In-situ observation of liquid water in operando fuel cells is possible. However identification of the parameters influencing the saturation evolution is very difficult because they are not easily accessible. To mitigate this problem an ex-situ experiment with well-controlled boundary conditions has been designed.

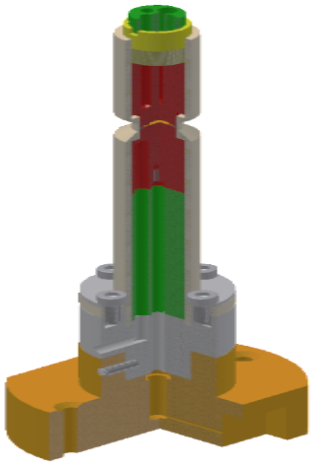

Figure 3: Rendering of the sample holder used for ex-situ liquid water imbibition/drainage in GDL

Liquid water can be stepwise injected in a compressed GDL at controlled capillary pressures using a syringe pump. For each pressure, a scan is performed and the corresponding 3D reconstructed images can be used to quantitatively determine the water content inside the GDL. With the segmented

structures it is also possible to observe where water is flowing preferentially. This information can be used to correlate the water transport to the microstructure of the GDL.

Figure 4 shows water invading the GDL progressively as the capillary pressure is increased. Between each segmented image the pressure is kept constant so that quasi-equilibrium is reached. Water saturation as well as the porosity can be locally calculated. These images serve as input for transport simulation in saturated GDL to derive effective transport properties. For example, the experimental data serves to confirm results of computed water imbibition predicted by the pore scale Monte Carlo model that is described in the next section.

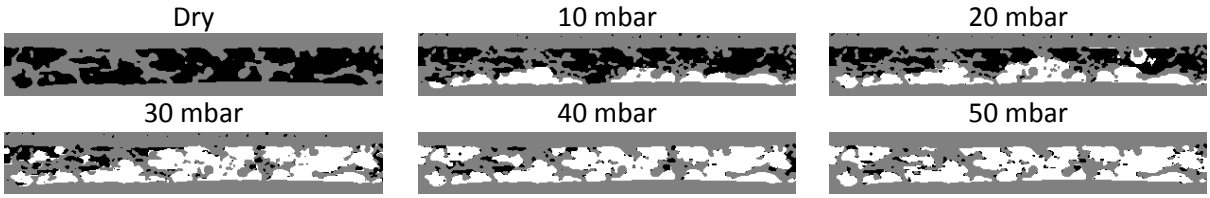

Figure 4: Segmented through-plane single slice of a SGL 25BA saturated at different capillary pressure. Black is void, gray is solid and white is water

Similar imbibition experiments will be be performed in other materials to assess the role of the microstructure on the transport processes (gas, water, heat, charge).

3.2. Pore-scale modeling of liquid water

3.2.1. Ensemble description of liquid water

In order to improve the efficiency and performances of polymer electrolyte membrane (PEM) fuel cells, the effect of the liquid water blocking the pores of the Gas Diffusion Layer (GDL) must be mitigated. Macro-homogeneous models treat porous media as an effective continuum involving volume-averaged quantities to find transport parameters such permeability and conductivity, while the effect of the water hindering the pores occurs at a lower scale.

Unfortunately, a significant length scale separation between the pore scale and the macroscopic scale is missing in GDLs, due to the small thickness of the GDL in comparison to the fiber diameter. Thus a multi-scale approach is needed to describe the influence of the pore-structure on the performance of the fuel cell.

We aim to model the liquid water distribution by a Monte Carlo (MC) approach, based on the surface free energy-based interactions among the different species voxel. The aim is to determine the equilibrium distribution of the liquid water, which in turn is used to calculate the macroscopic transport parameters.

Water clusters are generated by the electrochemical reactions in the catalyst layers. The water, the complex geometrical pore space defined by the porous structure are, together with the gaseous phase species, the three main constituents that need to be considered when modeling a GDL.
In order to distinguish those three phases, a proper meshing of the GDL domain is needed. A tradeoff between the size of the constitutive elements (voxels) and the computational effort is important. Each voxel is therefore provided with proper interaction energy, depending on the species, and is free to interact with the voxel within its Moore's neighborhood [1].
Since those interactions occur at the voxel level, collective behaviors such water aggregation and formation of water clusters are expected and the subset of the water voxels are treated as a classical statistical ensemble. Assuming the conservation of the amount of water, a canonical ensemble has been chosen. The probability of occurrence of a given spatial configuration of the water follows the Boltzmann distribution [2,6].
At the voxel scale, the water interacts with its neighborhood according to the probability defined by the Boltzmann distribution and the probability for the system to change its configuration as to move from the energy level E_i to E_j depends on their difference in energy.

It is worth to note that the movement, in the canonical framework, is to be intended as switching between the two interacting voxels, since the mass balance must hold.

3.2.2. Computational and modeling techniques

Simulating the liquid water based on ensemble statistical behavior, requires to mimic the transition from one spatial configuration to another via a Monte Carlo scheme. A simple but effective choice is to implement the Metropolis-Hastings algorithm [3,4], where the acceptance probability P_{acc} for each single move from the state E_i to E_j is calculated as [12]:

$$P_{i,j}^{acc} = \exp\left(-\frac{E_j - E_i}{k_B T}\right)$$

The notation $\beta = \frac{1}{k_B T}$ is used. Canonical ensembles allow to work in an isothermal framework and a normalization of different temperature-dependent parameters to the beta parameter is then used.

The Metropolis-Hastings Monte Carlo algorithm allows to generate a (stochastic) process of the states of the system which has no history dependence and it is called a Markov chain. That means the new configurations are generated with a probability that depends only on the current configuration and not on any previous configurations. The convergence to the equilibrium distribution requires additionally the ergodicity of the system, which basically means that starting from a given state, after a sufficiently large number of iterations, the system can visit all the possible configurational states: there are no unreachable configurational states [5,7].
In the proposed model, provided a sufficient number of iterations over the water voxels, the system converges to the equilibrium distribution which is shown to minimize the surface free energy of the water-solid-air system [8].

The energy of each voxel processed by the Metropolis-Hastings algorithm, is generally given by the sum of the interaction energies of its Moore's neighbors. The overall energy level for a given configuration is obtained summing over the energies of the single water voxels
By choice, the diagonal voxels are weighted as half of the edge-sharing ones. The interaction energy depends on how the material assigned to the voxels interacts with water at the interface (Figure 5). From a physical perspective, the work which has to be expended in order to form an interface with another species or phase (e.g. liquid on solid) is referred to as the surface free energy.

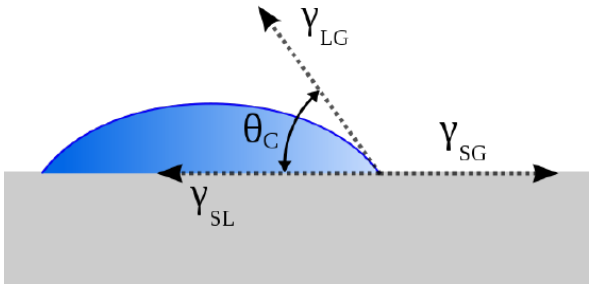

Figure 5: Contact angle and surface tensions at the three-phase interface

A more sophisticated model is needed for coming close to realistic simulations, as in the physical world the interface involves also the presence of air, which accounts for a third phase. Three surface energies are then to be considered which accounts for liquid-air, solid-air and liquid-solid interactions respectively [9,10,17]. The very feature defining the wettability property of the material is the difference of the surface tension of one interface compared to another. Macroscopically, the effect of the surface tension can be seen in the creations of a meniscus (e.g. in a capillary tube). The difference between solid-air and liquid-solid surface tensions can be either positive or negative, due to magnitude in different materials, therefore showing a typical concave or convex meniscus.
The shape of the meniscus is basically dependent on the definition of the contact angle of a liquid with a solid surface: the shape of a water droplet on a solid material is defined by the mechanical mutual restrains posed by the three surface tensions $\gamma_{lg}, \gamma_{sg}, \gamma_{sl}$ according to the Young's equation [11]:

$$\gamma_{sg} - \gamma_{sl} = \gamma_{lg}\cos(\theta)$$

where θ is the contact angle. The sign of $\gamma_{sg} - \gamma_{sl}$ is related to the hydrophobicity/hydrophilicity of the solid phase, as it changes the direction of the net force exerted between the solid and liquid phase. In the model developed, the interaction between voxels are assumed to be just pairwise.

From a thermodynamics point of view, calculating the energy of the water ensemble in the aforementioned way, deals only with the energetic cost needed to form a surface interface, accounting for the neighborhood's mutual influence. In the model, such a quantity is proportional to the Gibbs free energy per unit of surface. A proper weighting system accounting for the interaction surface is implemented.
Optimizing the computational performance when calculating such an interaction model, is crucial. While the structure of the porous media does not allow solid voxel switching, the intrinsic symmetry of switching gas and water voxels allows to iterate the algorithm only over the water voxels, which are indeed a small proportion of the overall domain discretization.
Indeed, the use of a non-local dynamics, known as Kawasaki dynamics [13], allows the simultaneous switching of all water voxels during a single Monte Carlo sweep, instead of sequentially attempting the

move for each water voxel as in the classical Glauber dynamics [14]. However, the simulation speed gained comes at the price that the intermediate steps of the algorithm, during the minimization procedure, does not give physical insight of the status of the system, until the quasi-equilibrium distribution is reached.

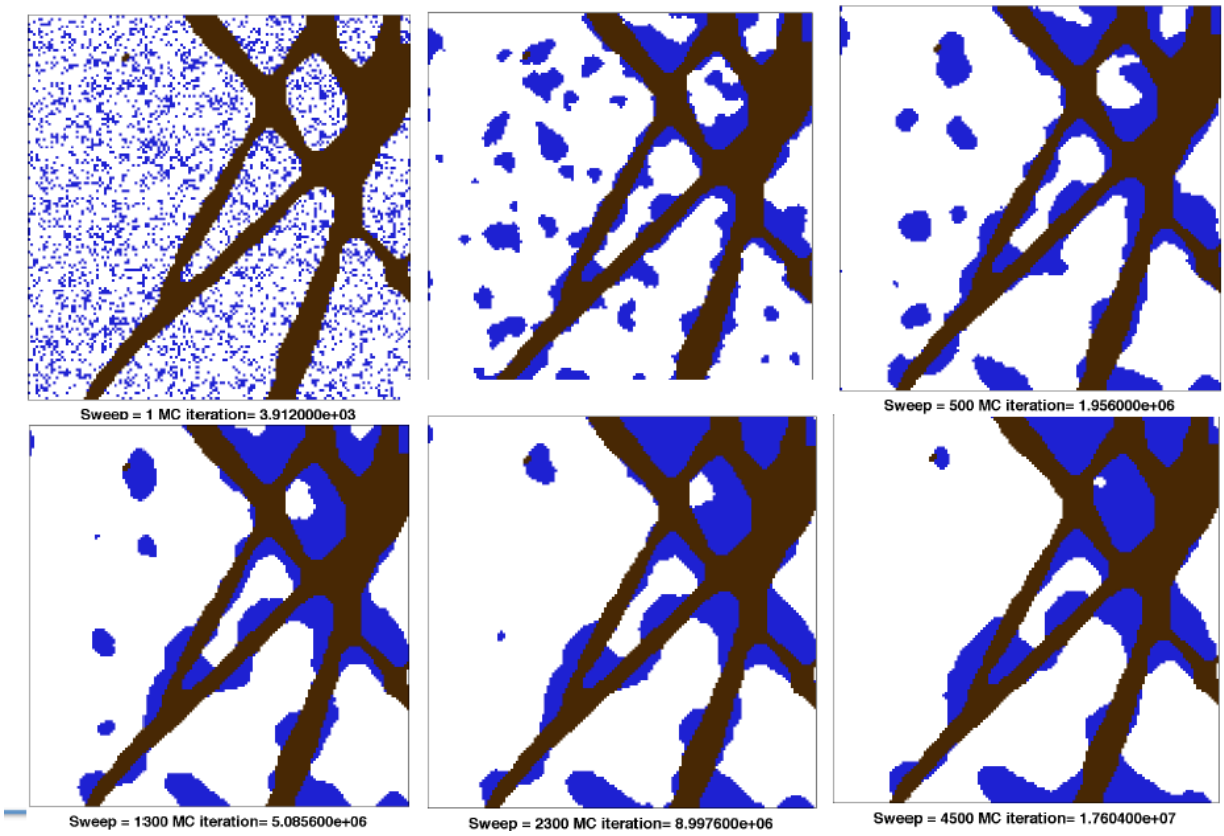

Figure 6: Water distribution at different MC iterations (from top left to bottom right). Water is shown in blue, solid is indicated in brown and void/air voxels are shown in white.

The starting water distribution is randomly distributed, given the volume. A sensitivity analysis has been performed with different random distributions as to assess the impact of the initial distribution on the final simulation results. In terms of energy of the water ensemble, different random seeds showed the same pattern as the system equilibrates: the surface free energy is minimized and the water distributes in way (Figure 6) which is energetically equivalent for all the randomized distributions. (Figure 7)

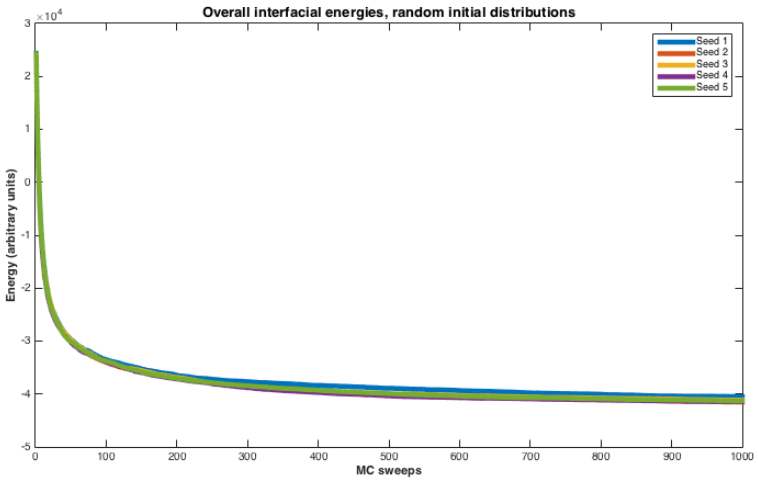

Figure 7: Energy pattern for different initial random distribution as function of MC iterations

3.2.3. Validation and results

The code FEMPS (Free Energy Monte Carlo Pore Scale) we developed, is able to calculate the equilibrium distribution of the water (EWD) in a given porous structure implementing the Metropolis-Hastings algorithm. A porous structure is required as an input and it can be randomly generated or imported from tomographic stacks or GeoDict virtual structures [15] either. The code developed so far, works on 2D layers.
By choosing the number of layers one wants to consider, an extension along the z-axis is supported, which practically leads to a 2D+1 framework for the code. Basically, the transmission mechanism between two consecutive layers, uses the EWD found at the *n*-th layer as the input for the *n+1*-th one. Such a mechanism, while rather simple, allows the water to behave in a quite physical way, being blocked by solid voxel and flowing through void ones.
Running the 2D Monte Carlo code layer by layer is convenient because of its computational speed but in principle there is no reason why the same scheme can not be applied to the whole 3D structure. Computational slowdowns will probably arise in this case, but few modifications would be required to the code.

An ideal capillary geometry has been used to benchmark the model and assess its behavior in a controlled environment where the shape (and particular the curvature radius) of the capillary was known. Pressure has been derived both analytically and numerically in two different models and compared against each other.
The analytical model is based upon the Young-Laplace equation [16], which relates the difference of pressure across the liquid interface (capillary pressure) with the total surface tension and curvature (in a straight planar capillary structure, $R_1 = R_2$) :

$$\Delta p = \gamma \left(\frac{1}{R_1} + \frac{1}{R_2} \right)$$

The numerical model relates the (average) pressure difference at the liquid-gas interface as a function of the different Gibbs energies of the phases and the effective surface area in contact with water (SA_C) :

$$\Delta p = \frac{\Delta G}{SA_C}$$

Fixing water content and temperature, a capillary-like geometry is considered, under periodic boundary conditions, to compare the outcome of the two models.

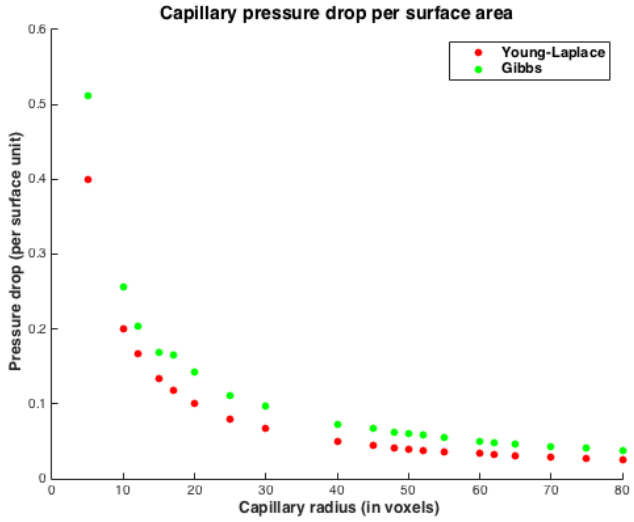

Figure 8: Pressure drop in an ideal tube as function of different capillary size

The formation of the characteristic (concave) meniscus and the evaluation of the pressure drop between liquid and gaseous phases shown in Figure 8 at different capillary size, shows a good agreement between the mechanical and statistical models proposed. Periodic boundary conditions and finite size effects, especially at small radii, can play a role in explaining the small deviations between the models. Nevertheless, shape, trends and physical interpretations for the pressure profiles are correctly represented.

After validating the code on a simple geometry, the simulations have been performed on the real GDL structures. Sets of dry and wet tomographic data of a SGL25BA sample have been provided by our partners at PSI and used as real geometries for running the Monte Carlo simulations at different water saturation levels (Figure 9 and Figure 10).

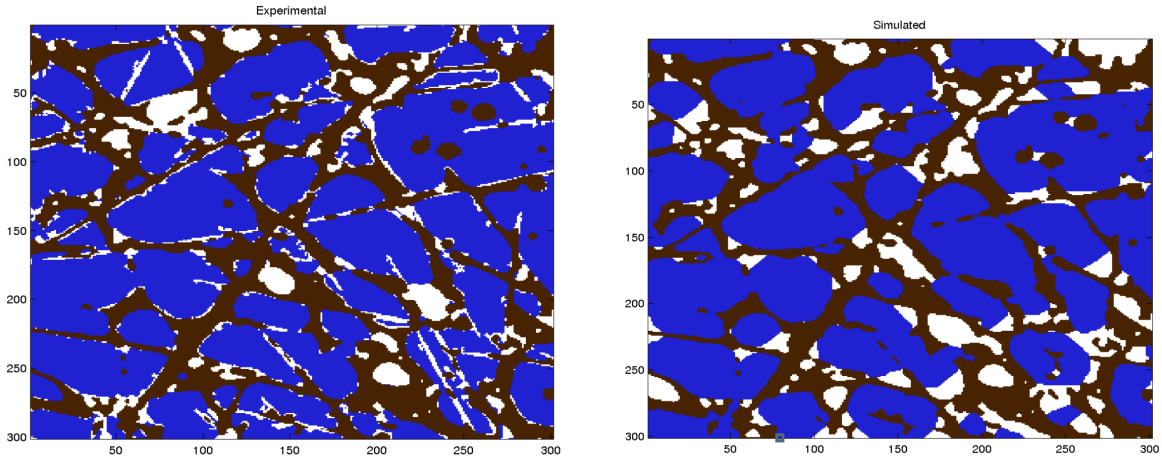

Figure 9: Experimental (on the left) and simulated (on the right) water invasion at the equilibrium in a SGL24BA GDL, p=50 mbar.

A visual comparison on those preliminary simulations, shows a good agreement between experimental data and simulations. The equilibrium water distributions are correctly captured in most of the pores and the water surface interaction is correctly captured (the solid phase is assumed to be graphite, which is hydrophilic).

Actually, the compound for the solid phase also contains a binder (which is hydrophobic) coming from the manufacturing process of the GDL, which is not captured by the tomographic apparatus and, during the segmentation phase of the image, happens to be labeled as solid or void, generating visual artifacts at the edges of the fibers.
Moreover, the experimental setup is intrinsically a 3D process in which the water is injected and imbibes the whole GDL.

A 2D inspection is easy, but does not take into account the presence of fibers on the top and bottom layers of the one that is inspected. That generates disconnections in the fibers representation and appearance of fiber-shaped void spaces, which the 2D simulation is inherently unable to reproduce. Further insight should be gained by developing a 3D Monte Carlo code.

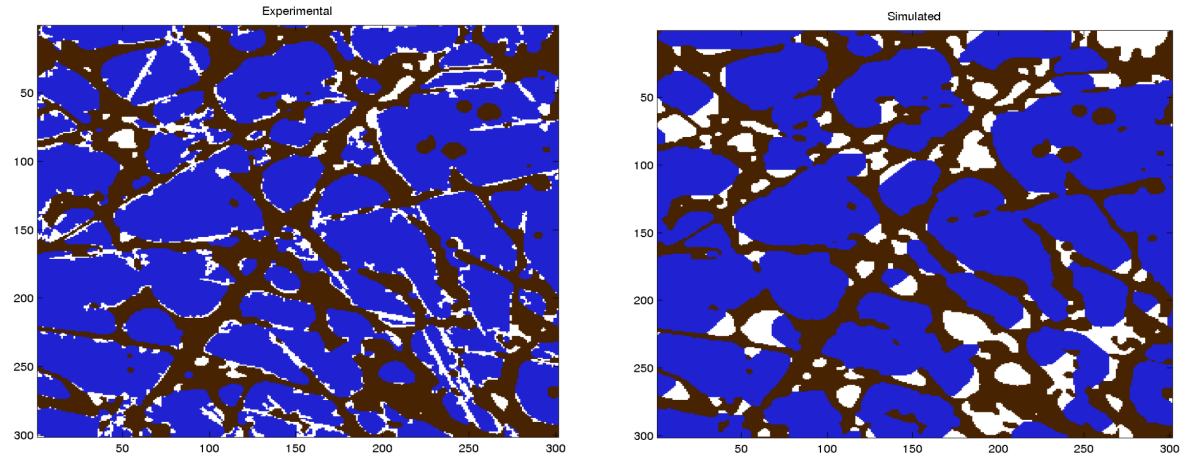

Figure 10: Experimental (on the left) and simulated (on the right) water invasion at the equilibrium in a SGL24BA GDL, p=100 mbar.

3.2.4. 3D pore-scale model of liquid water and effective transport properties

The Monte Carlo (MC) code for the modelling of liquid water in the GDL was extended to run on 3D domains. The code is first validated by modelling simple 3D cases like sessile droplets and capillary tubes, for which the results are well known. After this validation step, the equilibrium water distribution is simulated for a commercially available SGL 25BA GDL with 5 wt% PTFE loading and without microporous layer. Figure 11 shows the simulation result for a given average liquid water saturation of 40%, which corresponds to the experiment with an applied pressure of $p = 20\ \mathrm{mbar}$. The fibres are considered to be hydrophobic with an assumed constant contact angle of $\theta = 110°$. In order to account for the specific experimental conditions (water injection from the bottom, hydrophobic membrane on the top), non-symmetric top and bottom boundary conditions are used. Boundary conditions on the bottom prescribed a liquid water saturation of 100 % as to mimic the water invasion. The top boundary is prescribed to be a solid as to account for the hydrophobic membrane using the same contact angle as for the fibres.

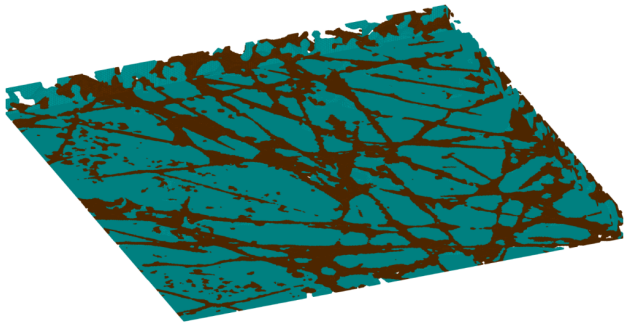

Figure 11: Simulated water invasion from the bottom, size 1126 µm x 1126 µm x 70 µm. Fibres in brown, water in blue.

In Figure 12 the differential in-plane images of the MC simulation and experiment are shown for the bottom, central and top slice of the micro structure. At the bottom slice (Figure 12, right), almost all the space is filled with water for both cases. Only some very small pores remain dry. The accessible pores are almost completely filled which means, that the hydrophobic fibres are totally included into the water cluster. Following the water path towards the hydrophobic membrane over the central (Figure 12, middle) and the top slice (Figure 12, left) one can observe that for the water injection experiment much less pores are accessible towards the top. Moreover, the accessible pores are no more filled completely and the hydrophobic fibres are included less into the water clusters. For the MC simulation, the water saturation decreases towards the top slice as well. At the central slice most of the pores are still occupied with water, but only a small fraction of the pores is filled and only few hydrophobic fibres are included into the water clusters. At the top slice near the hydrophobic membrane the water distribution is widespread and, in contrast to the experimental data, most pores contain some water.

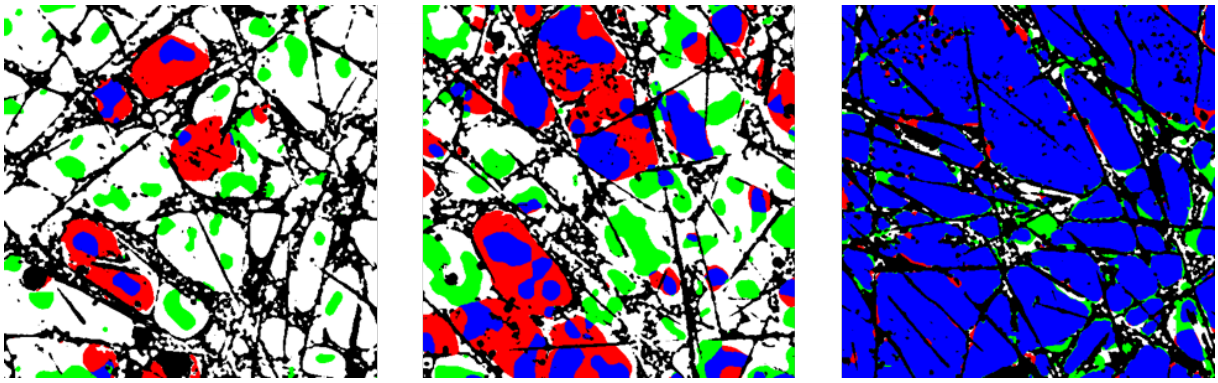

Figure 12: Differential picture of experiment and MC simulation. Fibres (black), water present for both cases (blue), water only in the experiment (red), water only in the MC simulation (green). Left) Top slice (hydrophobic membrane side). Middle) Central slice. Right) Bottom slice (water invasion side).

In a running fuel cell, water is transported along the liquid water pathways but also due to water vapour transport (i.e., phase change induced flow). The current hypothesis is that the two studied water distributions are the result of different dominant transport mechanisms: phase change induced water transport and condensation of water distributes the water; thereby the bottlenecks do not hinder the filling of smaller pores. This leads to a liquid water distribution according to the MC simulation results. On the other hand, the liquid water distribution obtained from the water injection experiment is governed by the bottlenecks of the pores, that is, the liquid water transport is dominated by the liquid pathways. However, this hypothesis still needs to be confirmed. While a study of the combined transport mechanisms on the pore scale is difficult, we expect to span the range of the transport properties by studying the two different situations where one of the two transport mechanisms is dominant.

For the MC simulation, the bottlenecks do not restrict the accessibility of the pores, but the water distribution is governed solely due to surface energy minimization, which is expected to describe the mechanism of condensing water vapour. As the algorithm is voxel based, it respects the real geometry very accurately and not only the pore and bottleneck size. This enables to capture the inclusion of the hydrophobic fibres into the water clusters near the water flooding boundary condition, which is also observed for the water injection experiment. This behaviour substantially affects the effective diffusion coefficient in the present case.

Regardless of the local physical behaviour of the water, since the ultimate goal is the upscaling from pore scale to the macroscopic scale for WP4, we are interested in the estimation of parameters needed to establish macro-homogeneous fuel cell models. For the comparison of the water distribution for the MC simulation and the experiment, non-symmetric boundary conditions were used for the MC simulation to reproduce as close as possible the conditions of the experiment. However, these boundary conditions are not necessarily appropriate for a running fuel cell. In order to examine the effect of different liquid water saturations on the effective transport properties, we therefore use the more basic symmetric boundary conditions for the MC simulation. In Figure 13, the in-plane averaged saturation profiles are plotted along the through-plane direction for the experiment and the MC simulation and for different average water saturations. The saturation curves from experiment show continuous gradient from the water injection side to the hydrophobic membrane side, while for the MC simulation with symmetric boundary conditions, the curves are more or less flat.

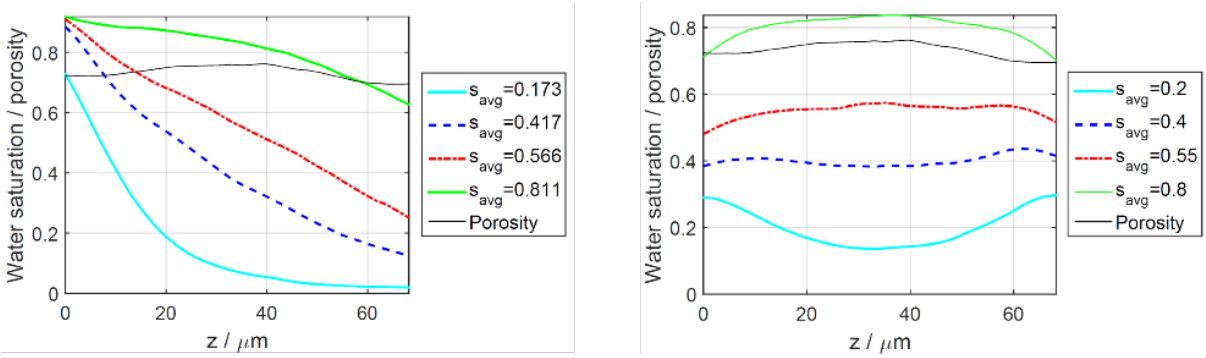

Figure 13: In-plane-averaged water fraction and porosity plotted along the through-plane direction for different average water saturations, (Left) for the water injection experiment, (Right) for the MC simulation with symmetric through-plane boundary conditions.

For comparison of the effective transport properties, the effective diffusivity and tortuosity for the gaseous species and the permeability of the liquid water pathways are calculated for both the MC simulation and experiment. Therefore, the modules DiffuDict and FlowDict of the software package GeoDict [1] were used. In this document, the discussion is restricted to the effective diffusivity for brevity. The effective diffusivity can be defined as the product of intrinsic diffusivity D_0 and a microstructure factor (M-factor) [3]:

$$D_{\text{eff}} = MD_0$$

The M-factor thus relates the effective diffusivity in the porous media with the intrinsic diffusivity of the gas accounting for all the microstructure effects relevant for the diffusion. To determine the M-factor, the fibres, the porous binder and the obtained water distribution for the two cases are treated to be fixed and impermeable for the gaseous species. According to this assumption, the gas can only diffuse through the void space which is not occupied by water, fibres and binder.

The in-plane (IP) M-factor, which is averaged for the two in-plane directions, and the effective through-plane (TP) M-factor are reported for MC simulation and experiment as a function of the average water saturation in Figure 14. While the in-plane values are quite similar for experiment and MC simulation, there is a big difference for the trough-plane values, especially for lower average water saturations. This result suggests that the effective diffusion properties for the gas phase are quite sensitive to a gradient in the liquid water saturation, while they are not much affected by the different in-plane distributions.

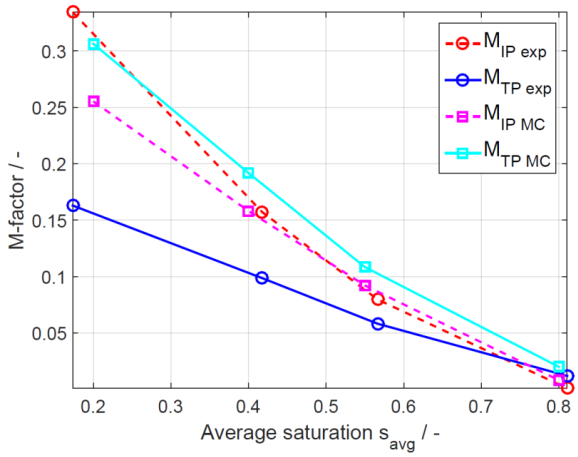

Figure 14: In-plane (IP) and through-plane (TP) M-factor for gas diffusion from Monte Carlo simulation (MC) and experiment (exp) for different average water saturations.

A manuscript on this topic has been accepted, the results discussed in this paragraph will be published by the ASME Journal of Electrochemical Energy Conversion and Storage [Capone 2017].

3.3. Microstructure analysis at the pore scale

The aim of work packages WP1 (dry GDL state) and WP2 (partially saturated GDL state) is to establish quantitative relationships between microstructure characteristics and effective transport properties for the porous layers in PEFC. The link between micro-characteristics and macro-properties is considered as a pre-condition for knowledge based optimization of these porous materials and for controlled water management in a low loss operation mode. Furthermore, a precise description of micro-macro relationships is needed as input for reliable macro-homogeneous modelling at the cell and stack levels (see WP4).

During the first project year we have used previously developed 3D methods for the investigation of effective properties in dry GDLs. These relationships allow us to predict effective properties (gas diffusivity, permeability, electrical conductivity) based on measured microstructure characteristics [3-4]. For dry GDLs the match between these predictions and independent measurements (via transport simulation) was fairly good. However, some uncertainties arose because of the following reason:

The fibrous GDL materials are highly anisotropic. Capturing the anisotropy by means of volume averaged parameters is not standardized for all characteristics of interest and therefore this issue requires special attention. In particular, it was not clear how the non-isometric cross-sections of the transport pathways can be described statistically, so that the corresponding transport limitations are captured correctly. It turns out that this issue is mainly relevant for the description of bottlenecks and hydraulic radii. Finding a solution to this problem can be the key to a fundamental understanding of the anisotropic transport properties and associated microstructure limitations. Solving these challenges was thus an important activity for WP1 in the reporting period.

A further important project goal (specific to WP2) is the description of relative permeability (of gas and liquid phases) depending on the state of saturation. Dedicated in-situ tomography experiments were performed at PSI, where water was injected gradually by increasing the pressure in controlled steps.

The above mentioned methods for establishing micro-macro relationships were then used to study the breakthrough behaviour (migration of the water front) and the relative permeability (steady state property as a function of saturation) under the view of potential microstructure limitations.

3.3.1. Completed tasks and achieved results for WP1

New quantitative relationships are established between effective properties (gas diffusivity, permeability and electrical conductivity) for a dry GDL (SGL 25BA) with the corresponding microstructure characteristics from 3D analysis. These microstructure characteristics include phase volume fractions, geodesic tortuosity, constrictivity and hydraulic radius. The latter two parameters include information from two different size distribution curves for bulges (continuous PSD) and for bottlenecks (MIP-PSD). X-ray tomographic microscopy is performed for GDL at different compression levels and the micro-macro relationships are then established for the in-plane and through-plane directions. The predicted properties based on these relationships are compared with numerical transport simulations, which give very similar results and which can be summarised as follows:

- Gas diffusivity is higher in the in-plane than in the through-plane direction. Its variation with compression is mainly related to changes of porosity and geodesic tortuosity.
- Through-plane permeability is slightly higher than in-plane. Permeability is mainly dominated by variations in hydraulic radius.
- Electrical conductivity is higher in in-plane direction than in through-plane. The anisotropy of electrical conductivity is controlled by tortuosity, which is higher for the through-plane direction.

Quantitative relationships are provided, which are considered to be more accurate and precise than older and more conventional descriptions (e.g. Carman-Kozeny, Bruggeman). The improved methods are based on detailed topological information from 3D analysis, whereas the conventional approaches make idealized assumptions about the microstructure. Furthermore, using these new relationships as input for macro-homogenous modelling enables to simulate microstructure effects of real GDL more accurately.

The outcome of these investigations in WP1 is summarised in a scientific publication [Holzer 2017a].

3.3.2. Completed tasks and achieved results for WP2

In WP2 liquid water transport in a commercial GDL (SGL 25BA) is investigated on the pore scale. X-ray tomography experiments performed at PSI combined with pressure-induced water injection provide 3D images of the liquid water distribution inside the GDL at incremental pressure steps between 0 and 100 mbar.

The breakthrough behaviour of the liquid phase is highly anisotropic. In through-plane (TP) direction first bubble points appear at the outlet plane already at 5 mbar and the 'breakthrough' then evolves continuously over an extended pressure range up to > 30 mbar as shown on the left side of Figure 15.

For in-plane (IP) direction the breakthrough is discontinuous and takes place at 27 mbar (see right side of Figure 15).

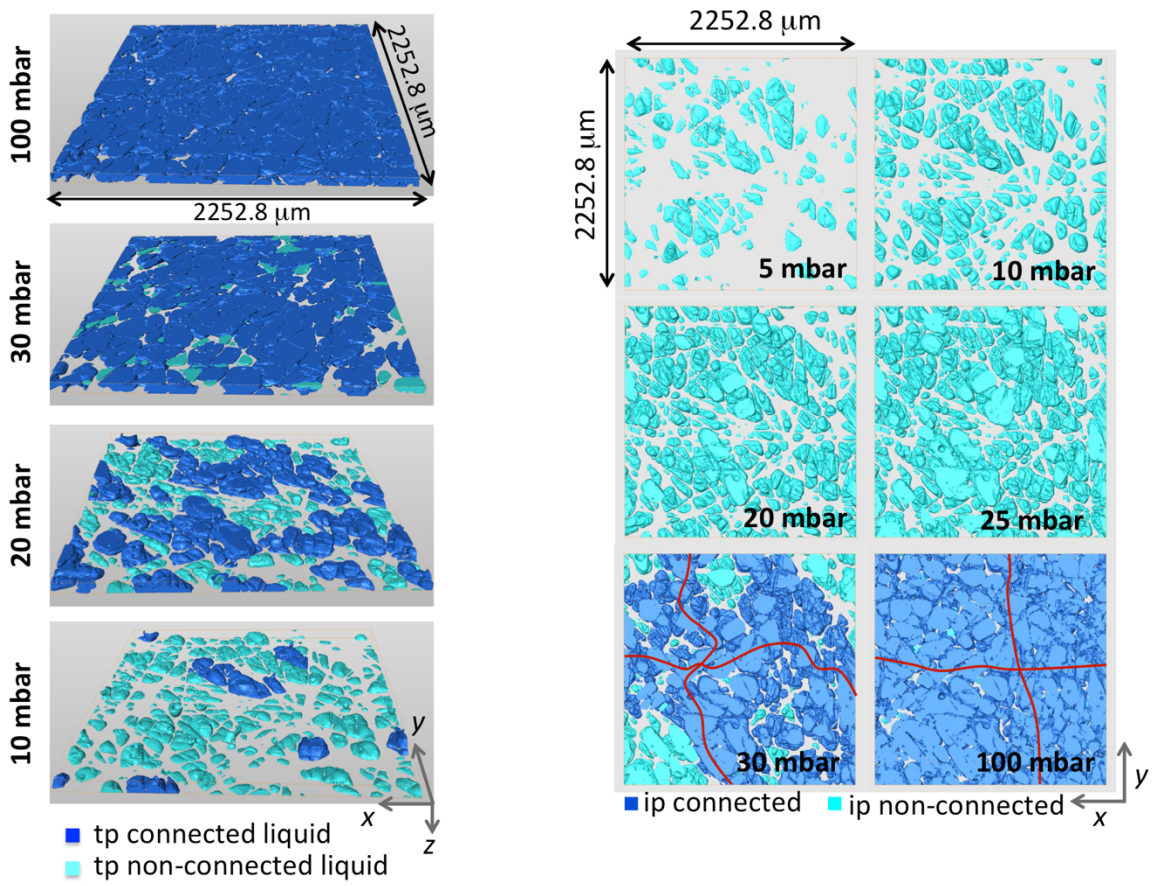

Figure 15: Visualization of the connectivity of liquid water, which is intruding the gas diffusion layer of a proton exchange membrane fuel cell from the bottom layer due to pressure induced injection. The images are acquired by means of X-ray-tomography. Fibres *and empty pores are not shown (transparent).*

Left: Through-plane. Light blue represents liquid clusters that are not connected with the top layer. Dark blue represents water clusters that are vertically percolating. The through-plane 'pseudo- breakthrough' evolves continuously over an extended pressure range from 5 to >30 mbar.

Right: In-plane. Light blue represents liquid clusters that have no in-plane connectivity. Dark blue represents water clusters that percolating in plane (e.g. from left to right or from top to bottom). The in-plane breakthrough is a discontinuous, abrupt event, that takes place at approx. 27 mbars.

Simulations of the intrusion process reveal that the different breakthrough behaviours are mainly triggered by different IP and TP transport distances. Short TP transport distances through the thin GDL (ca. 100 µm) are responsible for the characteristic continuous TP breakthrough behaviour, which is thus attributed to a short-range effect.

Quantitative relationships are established between the relevant microstructure characteristics and the liquid permeability, which provide a better understanding of the underlying microstructure limitations for injection and liquid transport.

For the in-plane direction the liquid permeability is limited to roughly a similar extent by tortuosity, constrictivity and effective volume fraction. In contrast, for through-plane direction relatively low volume fractions of the liquid phase put stronger limitations to the liquid permeability than tortuosity, constrictivity and hydraulic radius.

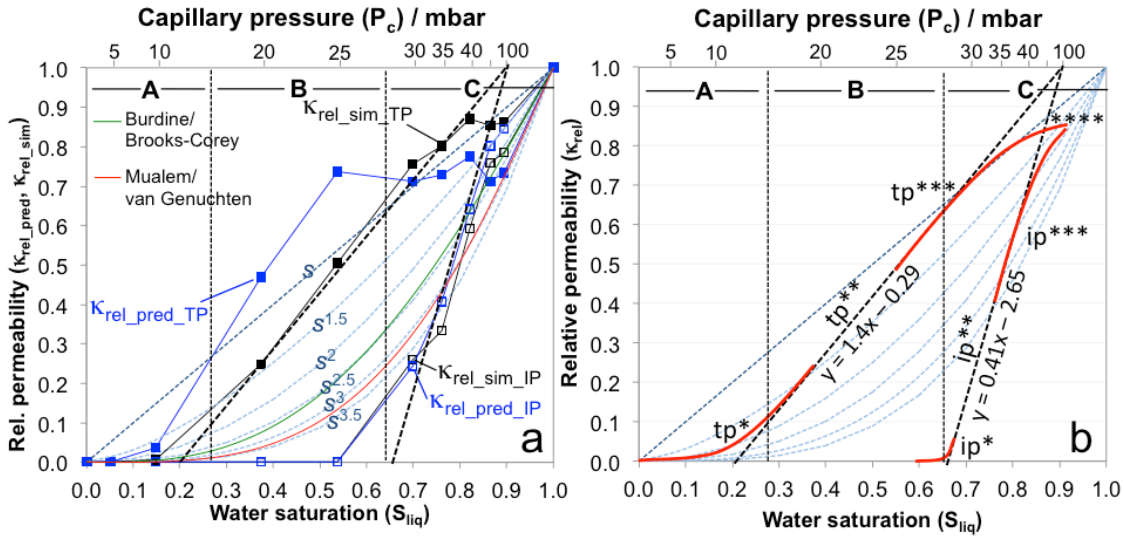

Figure 16: Relative permeability curves with complex S-shape are obtained both with predictions based on microstructure characteristics (micro-macro relationships) and with numerical 3D simulation. The complex shapes can be related to phenomena such as continuous breakthrough (concave segment for TP direction) and for example a drop in hydraulic radius at high saturations (convex segment for TP and IP directions). From [Holzer 2017b].

The curves for relative permeability vs. saturation (and vs. capillary pressure, respectively) achieved from 3D analysis reveal complex but characteristic (reproducible) shapes with concave, linear and convex segments (see Figure 16). The shape of these segments can be attributed to distinct microstructure effects. In contrast, the conventional macroscopic descriptions from literature cannot capture these complex shapes and the underlying microstructure effects. Future investigations with different GDL materials are necessary in order to understand whether these complex shapes for the relative permeability represent a general feature of GDLs or if they are specific to the investigated SGL material.

The main results from WP2 are summarised in a publication of Holzer [Holzer 2017b].

3.4. Influence of binder porosity on diffusion in GDLs

Precise characterization of the transport properties of GDLs is essential to properly assess and mitigate performance limitations of polymer electrolyte fuel cells. Within WP1 of this project, a Sigracet 24BA carbon paper material from SGL is investigated. The Sigracet materials contain porous binder. The influence of binder porosity on the GDL transport properties has not been analysed so far. Therefore, the GDL material is imaged using X-ray tomographic microscopy and segmented into a ternary structure of void, fibre and binder. A summary of extracted material properties is given in Table 1. With the resolution achieved (voxel edge length of 2.2 µm), binder porosity is not resolved. However, assuming different binder porosities i.e. different binder transport properties in the void and solid part of the binder, the effective diffusivity of the entire GDL material is numerically calculated.

*Table 1: Image-based characteristics of the SGL 24BA GDL. ROI: 3960 x 3960 x 202.4 µm3. *Data from manufacturer.*

	Volume fraction [%]	Mass density* [g/cm^3]	Area weight [mg/cm^2]	Solid mass fraction [%]
Binder	14.9	1.7	5.2	64.1
Fibre	8.0	1.8	2.9	35.9
Solid	22.9	-	8.1	100
Void	77.3	-	-	-
Total	100	-	-	-

The results indicate that the binder characteristics have a significant impact on the overall GDL diffusivity. Figure 17 shows grey scale in-plane and through-plane slices as well as their corresponding segmentations for SGL 24BA. The separately segmented fibres (green) and binder phases (red) can clearly be identified.

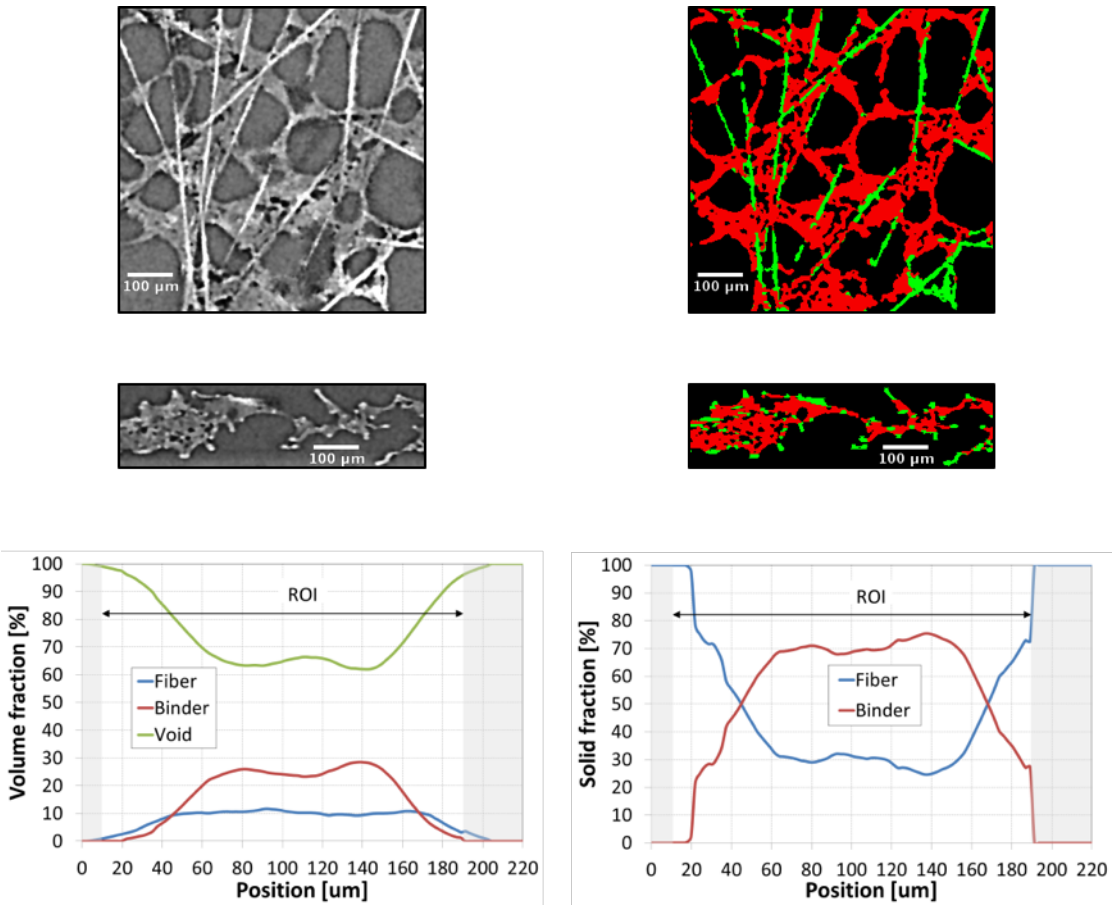

Figure 17: Top and middle, left: in- and through-plane slices of a reconstructed uncompressed SGL 24BA GDL. Top and middle, right: corresponding segmented slice; red colour corresponds to binder and green to fibres. Bottom left: volume fraction distribution acros across the GDL thickness obtained from segmented imaging data. Bottom right: solid fraction distribution across the GDL thickness.

The volume fraction distribution indicates a heterogeneous porosity of the GDL across the thickness, with a higher porosity in the centre of the GDL [9]. The differentiation between binder and fibre reveals that

- the fibre content is approximately constant across the thickness of the material,
- the binder volume fraction is considerably higher than that of the fibres (about 65:35) and is responsible for the higher porosity in the centre of the material,
- the outer surfaces are mainly consisting of fibres.

To investigate the influence of the binder morphology on gas transport, simulations using the ternary structure are performed with variation of the binder properties. In Figure 18, the GDL effective diffusion coefficient $D_{\mathrm{eff}}^{\mathrm{GDL}}$ is plotted as a function of the binder effective diffusion coefficient $D_{\mathrm{eff}}^{\mathrm{B}}$. The latter ranges from 0 to 1 corresponding to diffusion in the solid and open space, respectively. The property of the binder has a significant influence on the diffusion in the void: $D_{\mathrm{eff}}^{\mathrm{GDL}}$ varies by about a factor of 3 for the full binder property span.

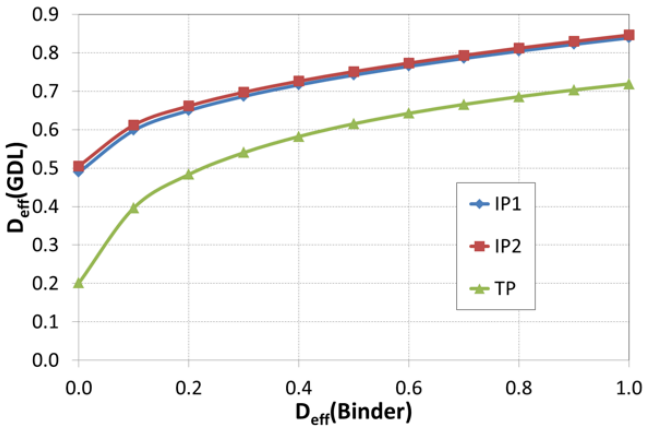

Figure 18: In-plane and through-plane effective diffusivity vs. binder diffusivity of the GDL.

The calculations are performed for the three orthogonal space directions: two in the in-plane and one in the through plane direction. The diffusion coefficient is lower for the through-plane direction and a small anisotropy is observed for the in-plane directions. The higher through-plane than in-plane void tortuosity is responsible for the diffusion anisotropy [Holzer 2017a]. The anisotropy appearing between the two in-plane directions may stem from the manufacturing process. This anisotropy is limited to about +/- 3%.

Future work will focus on the influence of the porous binder on the solid phase transport and of compression and PTFE loading on the transport properties of GDLs. It will remain the operando characterization of the small pores in the binder, as they may play a significant role in the supply of reactants to the catalyst layer at high liquid water saturation of the macropores in the GDL.

3.5. Droplet release from GDL to the gas channel

3.5.1. Experimental results

When droplets appear at the surface between GDL and gas channel, they detach as a result of the shearing force exerted by the gas flow. This detachment is supposed to have a significant influence on the liquid saturation in the pores of the GDL, influencing local cell performance. Using fast X-ray tomographic microscopy, the behaviour of the saturation at droplet removal is investigated in work packages WP3. A first round of preliminary experiments has been completed and a second iteration with improved precision control is currently in process at PSI as of December 2016.

3.5.2. Preliminary results

Figure 19 shows the capillary pressure increase necessary for the water to penetrate the GDL. When the water reaches the gas channel, a sudden capillary pressure decrease is observed. In

Figure 20, preliminary X-ray tomography images of water are shown before penetration of the GDL (left) and at maximum capillary pressure (right).

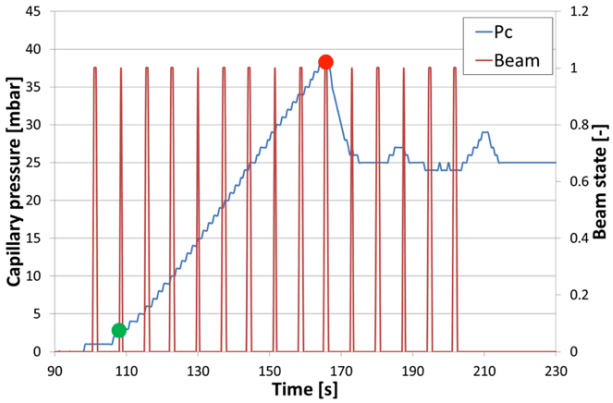

Figure 19: Experimentally observed capillary pressure evolution during liquid water injection in a Toray TGP-H 060 GDL at 30 µl/min. The air velocity in the gas channel is 6.9 m/s.

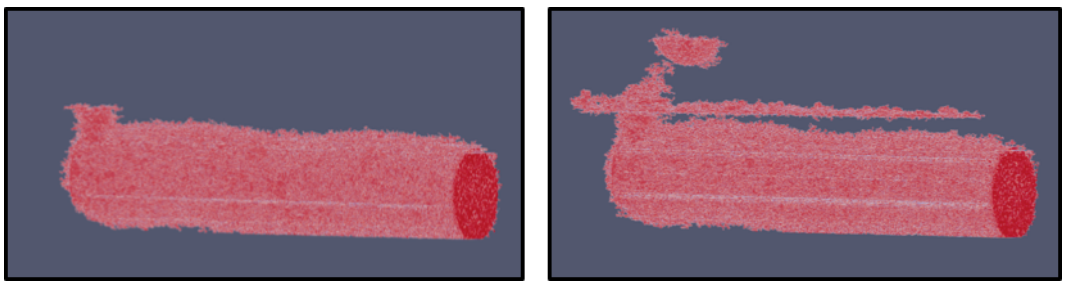

Figure 20: Liquid water before penetration (left) and at maximum capillary pressure (right) during water injection in a Toray TGP-H 060 GDL at 30 µl/min. The air velocity in the gas channel is 6.9 m/s.

3.5.3. Computational and analytical model

Droplet forming at the GDL/CH Interface

The interfaces between the different layers often play a dominant role because of the thinness of the layers. At the interface between the gas diffusion layer (GDL) and the gas channel (CH), water droplets are formed at the hydrophobic surface of the GDL. Within the work package WP3, this interfacial mechanism is studied and eventually included in macro-homogeneous PEFC models for WP4.

In Figure 21 the forming of a droplet at the top of a hydrophobic pipe is shown for the different geometrical sections. This is a strongly idealised situation compared to the complex fibre structure of the GDL with inhomogeneous local contact angle due to fibres, binder and PTFE spreading. Nevertheless, this model enables to study the basic physics involved. The model may be also quantitatively accurate when using appropriate effective parameters extracted from experiments.

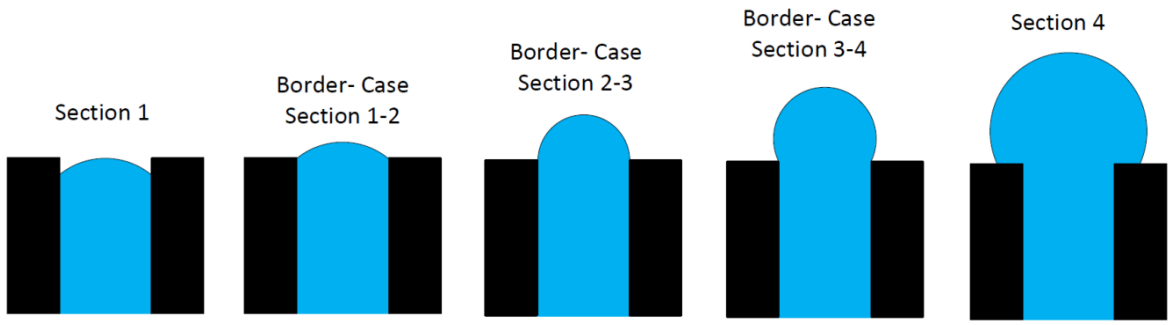

Figure 21: Idealized droplet forming at the GDL/CH interface.

To form the droplet, a sufficient interface pressure is needed according to the Young-Laplace equation $\Delta p = 2\gamma/r$. Thus, an appropriate interface pressure can be defined as a function of the geometrically defined instantaneous droplet radius. The evolution of the capillary pressure while forming a droplet according to Figure 21 is shown in Figure 22. The highest pressure occurs between Section 2 and 3, where the droplet forms exactly a half-sphere and obtains its minimal radius during the formation.

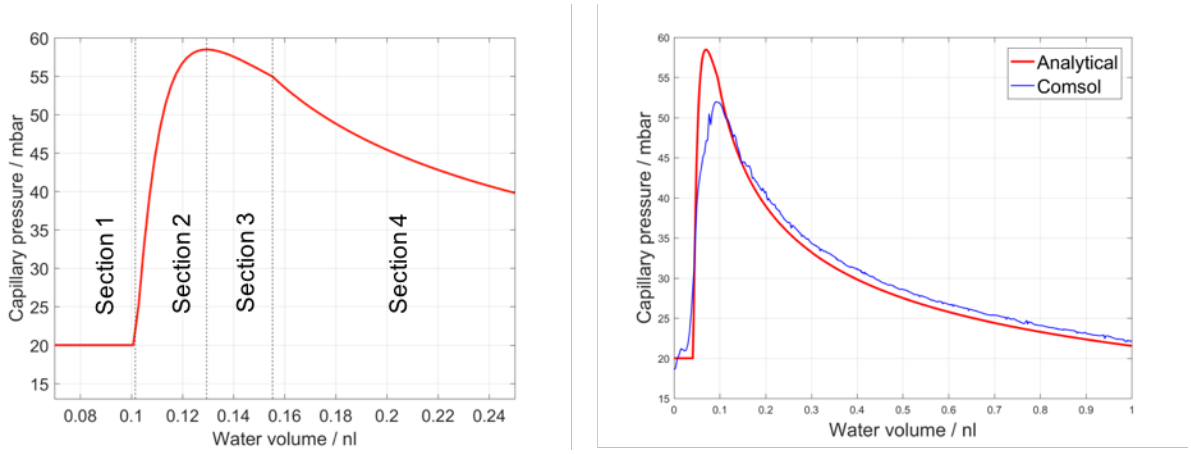

Figure 22: Left) Capillary pressure during drop formation. Right) Capillary pressure for the analytical model and the numerical two-phase model.

To validate the assumed idealized droplet forming, a two-phase CFD model has been implemented in COMSOL Multiphysics [7]. The model uses a Level-Set function to represent the interface between water and air including the effects of surface tension. The results of the axial symmetric simulation are shown in Figure 23 for the same situations as for the analytical forming in Figure 22, with very good agreement with the theoretical model. A comparison of the capillary pressures during the droplet forming is shown in Figure 22 on the right hand side. The qualitative behaviour of the capillary pressure is fully reproduced. The peak pressure is lower for the two-phase simulation, probably due to the spatial extension of the liquid-air interface of the CFD simulation.

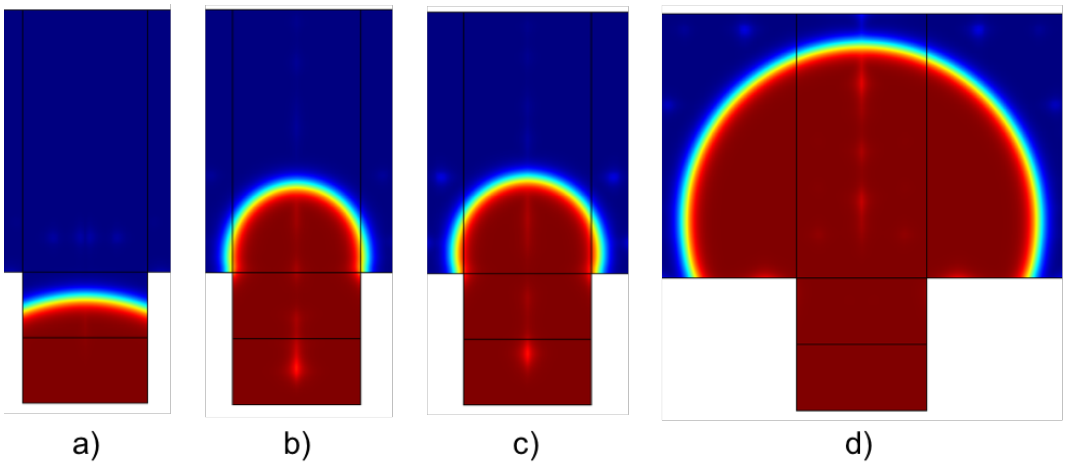

Figure 23: COMSOL two-phase model for the droplet forming at the GDL/CH interface. a) Section 1. b) Border case Section 2-3. c) Border case Section 3-4. d) Section 4.

Release of the droplets from the GDL surface to the channel

The water is transported in the gas channel due to different mechanisms [8]. In the following model, the liquid water transport in the channel is restricted to removal of water droplets by the gas stream which are then transported as a mist with the gas stream of the cathode channel.

Zhang et al. [8] proposed a model for the water removal from the GDL to the channel by detachment of water droplets. The diameter of the drop when it is removed from the GDL surface is determined as a function of the gas stream velocity in the channel. In Figure 24, this power-law prediction is plotted. In combination with the droplet forming model introduced above, a simplified but consistent model for the GDL/CH interface can be formulated for the macro-homogenous model, which is discussed in the next section.

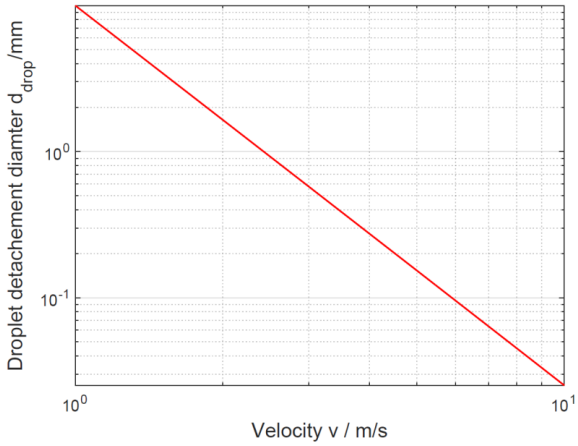

Figure 24: Droplet detachment diameter as a function of the channel flow velocity.

3.5.4. Transient macro-homogeneous simulation

The macro-homogeneous model for the water transport in the CL and GDL can be combined with the suggested interface model for the GDL/CH interface using a transient formulation. The continuity equation then reads

$$\frac{\varepsilon_0}{V_\mathrm{w}}\frac{\partial s}{\partial t} + \nabla \cdot \left(-\frac{\kappa}{\mu_\mathrm{w}}\nabla p_\mathrm{c}\right)\frac{\varepsilon_0}{V_\mathrm{w}} = Q_\mathrm{pc} + Q_\mathrm{R}$$

where ε_0 is the porosity of the dry GDL, s the water saturation, κ the permeability of the GDL, μ_w the viscosity of water, V_w the molar volume of water, p_c the capillary pressure in the GDL, Q_pc the evaporation and condensation source term and Q_R the source term for water vapour production due to the reaction, which is nonzero only in the CL. The boundary condition for the GDL/CH interface is formulated as

$$(\vec{n} \cdot j_s) = -\max\left(-\frac{\kappa_\mathrm{B}}{\mu_\mathrm{w} V_\mathrm{w}}\left(p_{\mathrm{c\,GDL/CH}} - p_\mathrm{c}\right), 0\right)$$

where κ_B is the permeability of the GDL/CH interface and $p_{\mathrm{c\,GDL/CH}}$ is the interface pressure governed by the capillary pressure of the droplet forming at the GDL/CH interface. Thus, water can only leave the GDL toward the channel if the capillary pressure in the GDL is higher than the capillary pressure of the droplet which is formed at the interface.

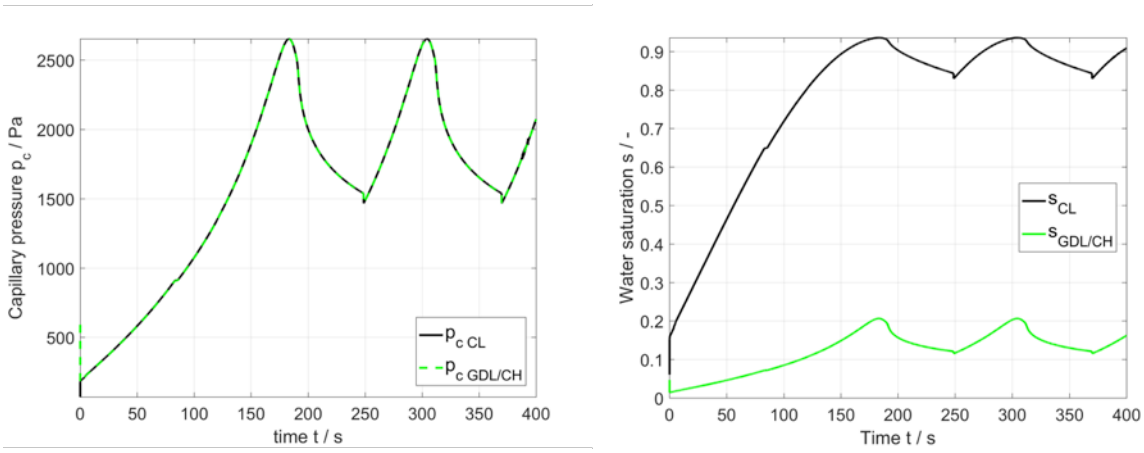

Figure 25: Left) Capillary pressure at the CL ($p_{c\,CL}$) and at the GDL/CH interface ($p_{c\,GDL/CH}$). Right) Saturation at the CL (s_{CL}) and at the GDL/CH interface ($s_{GDL/CH}$).

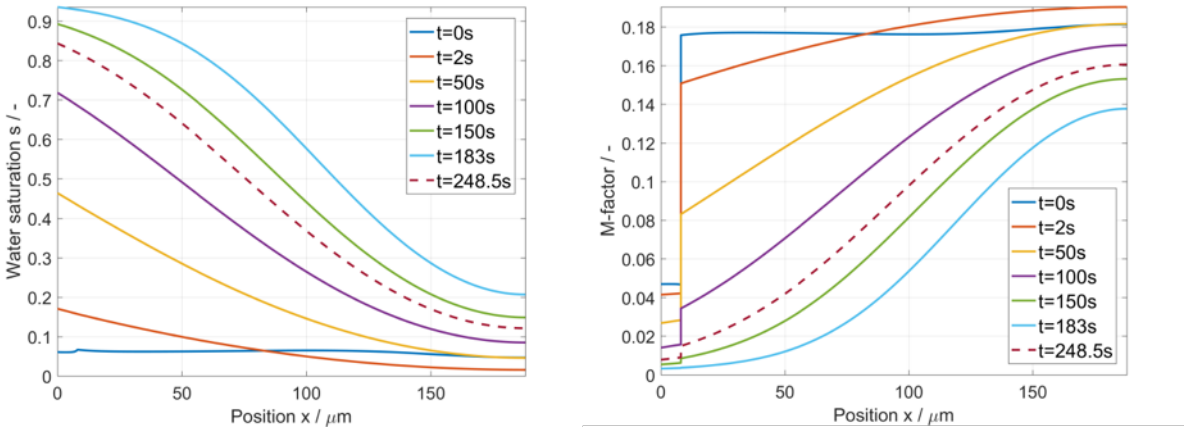

Figure 26: Left) Liquid water saturation profiles at different times. Right) Local M-factor at different times.

The capillary pressure of the GDL/CH interface $p_{c\,GDL/CH}$ is thus governed by the capillary pressure of the forming droplet and therefore varies over time as shown in Figure 25 on the left hand side. At the time $t \approx 250$ s, the droplet is detached from the top of the GDL into the channel (according to the implemented model of Zhang et al. [8]) and a new droplet starts to form. The capillary pressure at the CL $p_{c\,CL}$ shown in Figure 25 (left) almost falls on the curve of the interfacial pressure $p_{c\,GDL/CH}$, as there is only a very small pressure drop along the CL and GDL due to the very high permeability. Due to the variation of the GDL's capillary pressure, also the saturation varies with time as shown in Figure 25 (right) where the saturation of the CL and of the GDL/CH interface is plotted over time. In Figure 26 (left), the saturation profile in trough-plane direction is shown for different times. The artificial initial condition at $t = 0$ s evolves to the characteristic saturation gradient shown at $t = 2$ s. The water produced due to the reaction can leave the GDL only by overcoming the interface pressure due to the droplet forming. The saturation in the GDL therefore increases according to the capillary pressure / saturation curve of the GDL material. After reaching the maximal interface pressure at $t = 183$ s, the saturation in the GDL decreases along with the decreasing interface pressure. In Figure 25 (right), the local M-factor, which is a measure for the local diffusivity, is plotted for the same times as the saturation profiles. The M-factor decreases with increasing saturation and shows also a strong gradient. The alteration of the diffusivity in time will also affect the fuel cell reaction and thus cause local fluctuations in the current-voltage behaviour. For the whole cell, these fluctuations will mostly be averaged out. The current simulation thus shows the result for a control volume including one dominant percolation path with a corresponding droplet forming at the GDL/CH interface.

The GDL/CH interface model shall be validated with the transient tomography measurements which are currently in process at PSI to complete WP3. Moreover, more appropriate models for the CL/GDL and MPL/CL interface may need to be developed. The different model improvements will then be implemented in a macro-homogeneous membrane electrode assembly model including all the important processes involved in a fuel cell, which is currently being developed at ZHAW-ICP.

3.6. Fully parameterized 1D MEA model

The purpose of this working task was to develop a fully parameterized macro-homogenous, non-isothermal, steady-state membrane electrode assembly (MEA) model including gas diffusion layers

(GDLs) for low-temperature proton exchange membrane fuel cells (PEMFC) that reflects current state-of-the art modeling in the sense that:

- it uses latest experimentally determined constitutive relationships and fully parame- terized material properties that are applicable to modern MEA materials
- it uses effective material properties such as permeability and diffusion coefficients based on the microstructure analysis of this project (M-factor)
- it includes the effects of axial compression on effective material properties and overpotential
- it includes the effects of electrical and thermal contact resistance as a function of compression
- it includes the latent heat of water evaporation/condensation and membrane sorption
- it accounts for the different water uptake and release of the membrane from/to liquid and vapor (Schroeder's paradox)
- it includes thermo-osmosis of water through the membrane
- Neumann boundary conditions are formulated for the water transport to reflect realistic operating conditions as closely as possible
- gas transport is properly modeled using Knudsen diffusion and the Stefan-Maxwell model

The model was implemented in COMSOL Multiphysics with LiveLink for MATLAB.

3.6.1. Modeling domain

In the one-dimensional PEMFC model developed here, the membrane electrode assembly (MEA) is represented as a series of five adjacent homogeneous interval subdomains representing a cell-area-averaged through-plane section of the porous layers of a fuel cell. It includes the proton exchange membrane (PEM) in the middle, sandwiched by two catalyst layers (CLs) and two gas diffusion layers (GDLs). The gas channels and mono- or bipolar plates on either end are modeled as boundaries of the MEA.

The geometry of the MEA model is shown in Fig. 1. The five subdomains (layers) are labelled Ω_i, i = 1, .., 5 with boundaries $\partial\Omega_i$, i = 1, ..., 6. For the specification of Neumann boundary conditions (BCs), the interface director $\vec{n}$ is defined to be the outward-pointing normal vector. The thickness of the different layers comprising the MEA ($L_{\Omega i}$) are rescaled to unit length in the illustration. Note that currently, the microporous layer (MPL) is not explicitly represented in the model.

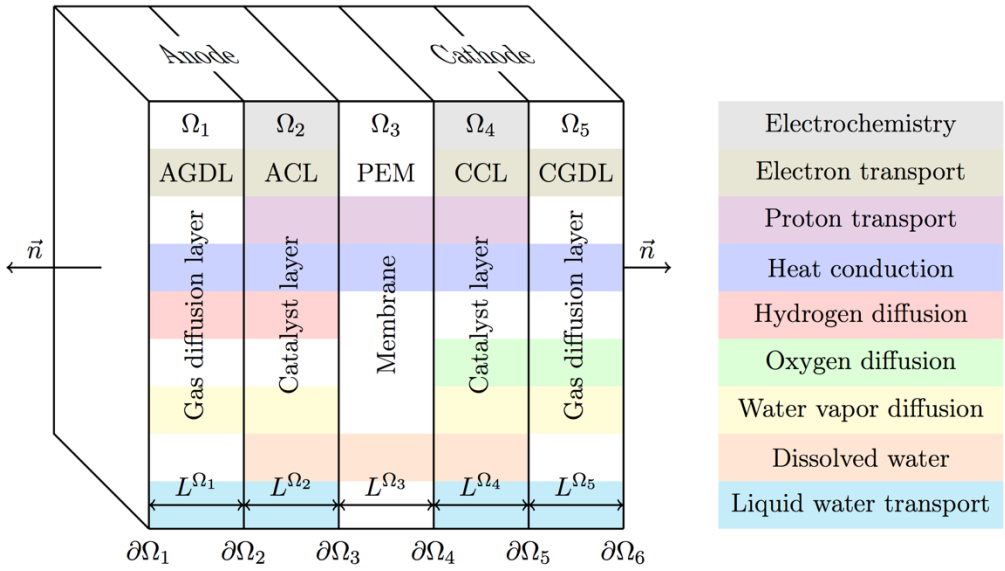

Figure 27: Idealized geometry of the PEMFC model. The individual subdomain lengths LΩi , i = 1, ..., 5 are not shown to scale. Different physical transport processes are taken into account in different subdomains as marked in color.

3.6.2. Brief model description

This is a brief summary of the membrane electrode assembly model that has been developed in the project. A detailed model report of the ICP is available[1] including all governing equations, constitutive equations, boundary conditions, and references used.

The *electrochemical reactions* in the catalyst layers are described by Butler-Volmer equations, where the amount of platinum surface per unit volume of the CL is taken into account. The reversible half cell potentials of the anode and cathode are modelled by the Nernst equations.

To model the *transport of charge, heat and mass* we follow the continuum approach and describe the most dominant transport processes of charge, energy, gas species and water by conservation laws. This results in eight coupled second-order partial differential equations (PDEs) representing conservation equations of charge (electrons and protons), heat, gas species (oxygen, hydrogen, water vapor), dissolved water in the polymer electrolyte, and liquid water in the porous layers. These conservation equations are summarized in Tab. 1 for the steady state.

[1] R. Vetter, P. Marmet, L. Capone, J.O. Schumacher. Internal project report of the Team Electrochemical Cells and Energy Systems: PEM-NFP70 “Designing multifunctional materials for proton exchange membrane fuel cells”, Institute of Computational Physics, ZHAW. Version: November 2017.

Table 2: Governing equations of the membrane electrode assembly model.

Name	Dependent var.	Flux	Continuity equation
Ohm's law for electrons	ϕ_e	$j_e = -\sigma_e \nabla \phi_e$	$\nabla \cdot j_e = S_e$
Ohm's law for protons	ϕ_p	$j_p = -\sigma_p \nabla \phi_p$	$\nabla \cdot j_p = S_p$
Fourier heat conduction	T	$j_T = -k \nabla T$	$\nabla \cdot j_T = S_T$
Water transport in ionomer	λ	$j_\lambda = -(D_\lambda / V_m) \nabla \lambda + (\xi / F) j_p$	$\nabla \cdot j_\lambda = S_\lambda$
Fickean water vapor diffusion	x_{H_2O}	$j_{H_2O} = -C D_{H_2O} \nabla x_{H_2O}$	$\nabla \cdot j_{H_2O} = S_{H_2O}$
Fickean hydrogen diffusion	x_{H_2}	$j_{H_2} = -C D_{H_2} \nabla x_{H_2}$	$\nabla \cdot j_{H_2} = S_{H_2}$
Fickean oxygen diffusion	x_{O_2}	$j_{O_2} = -C D_{O_2} \nabla x_{O_2}$	$\nabla \cdot j_{O_2} = S_{O_2}$
Liquid water transport (Darcy)	s	$j_s = -(\kappa / \mu V_w)(\partial p_c / \partial s) \nabla s$	$\nabla \cdot j_s = S_s$

In the CLs and GDLs, Ohm's law is assumed to govern how the flux of electrons je is driven by a gradient of the electronic phase potential. The analogous equation is used for the flux of protons j_p within the electrolyte phase of the CLs and the membrane. The two electrostatic phase potentials φ_e and φ_p coexist in the CLs (see Figure 28), defining $\Delta\varphi$ in these two domains. The approach is adopted from the classical porous-electrode theory of Newman, where it is assumed that the electric double layer constitutes only a small volume compared to any of the phases or the electrode itself [35].

Heat conduction is the dominating mode of energy transport in the MEA, allowing for an accurate description of the heat flux j_T by Fourier's law in all five subdomains. This is the third differential equation.

The description of water balance in the ionomer is based on the seminal model by Springer et al. [45]. To represent the degree of humidification, the number of water molecules per acidic group λ is usually used. The molar flux of dissolved water j_λ is composed of the sum of its two most significant contributions: back diffusion due to a moisture gradient ($j_\lambda \sim -\nabla\lambda$) and electro-osmotic drag ($j_\lambda \sim j_p$). The next three equations are dedicated to the transport of gas species on both sides of the membrane. If gas crossover is neglected, it is sufficient to consider hydrogen only on the anode side and oxygen on the cathode side, whereas water vapor is present in both gas mixtures. A third gas component is implicitly accounted for on either side (typically nitrogen if air is supplied to the cathode) and need not explicitly be computed because the sum of mole fractions is equal to one everywhere. We assume uniform gas pressure P in the steady state, and hence the dominant transport mechanisms is inter-diffusion of the gas species. Thermal diffusion, as it results from the chemical potential gradient as the general driving force for species transport, is neglected. The ideal gas law is used to calculate the interstitial gas concentration.

Finally, for the description of liquid water transport, we adopt the unsaturated flow theory that was carried over from soil physics to the fuel cell modeling community by Natarajan & Nguyen [34], and which has since become the de-facto standard in macro-homogeneous two-phase MEA modeling. Darcy's law is transformed into an equation for liquid water flux driven by a gradient ∇s, where s denotes the liquid water saturation (fraction of pore space filled with liquid water). This requires the specification of both the saturation-dependent hydraulic permeability κ and the differential relationship between the capillary pressure and saturation, ∂pc/∂s, as material properties.

For each of these eight fluxes, a continuity equation is expressed in the last column of Table 2, equating the divergence of each flux j with a corresponding source term S. These eight PDEs become nonlinear when the coefficients and/or source terms are expressed in terms of the dependent variables. All phase transitions and reaction rates appear as sources that couple these PDEs.

3.6.3. Base case simulation results

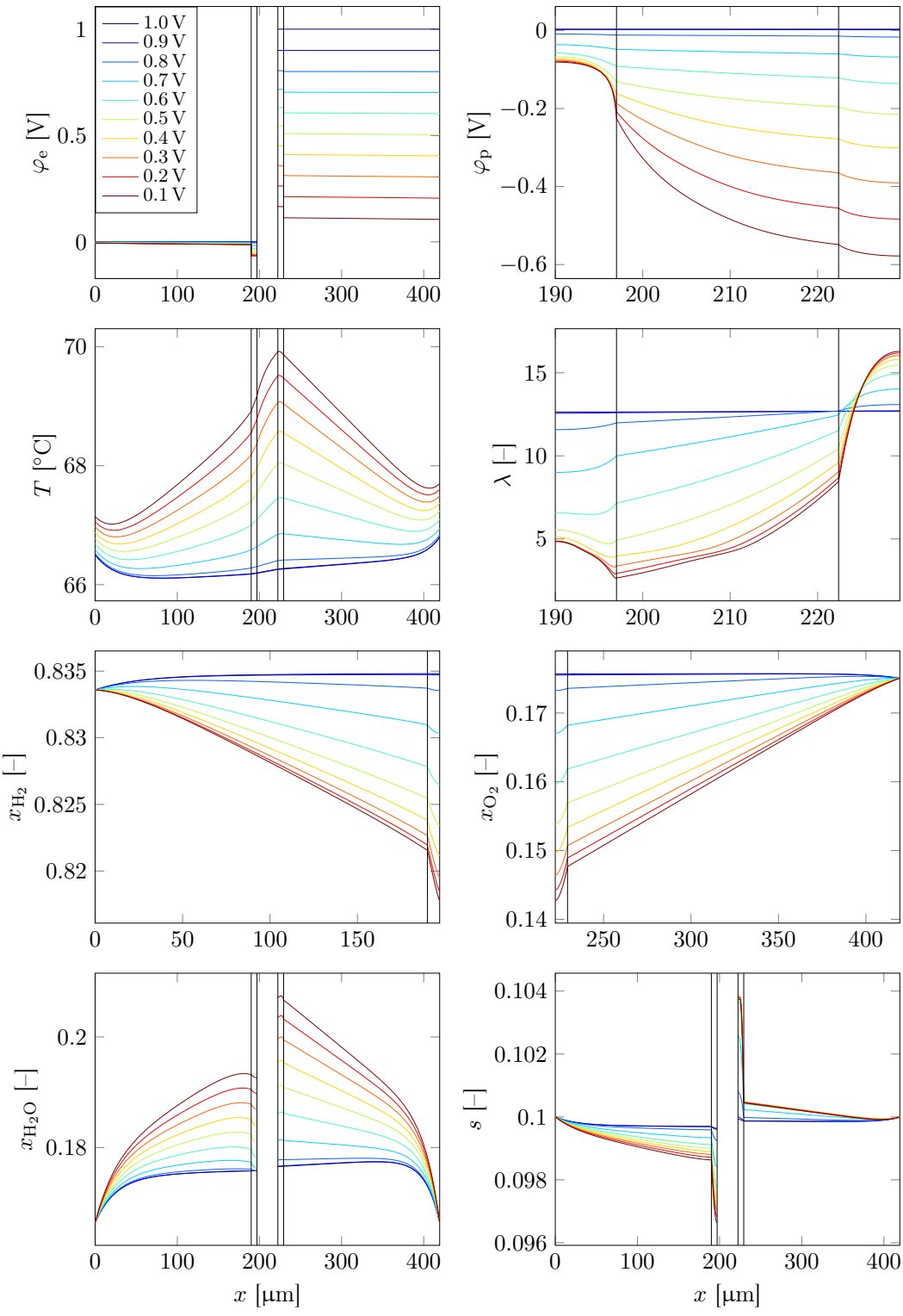

Figure 28: Local distribution of the potential variables that drive the fluxes of electrons, protons, heat, dissolved water, hydrogen, oxygen, water vapor, and liquid water through the membrane electrode assembly.

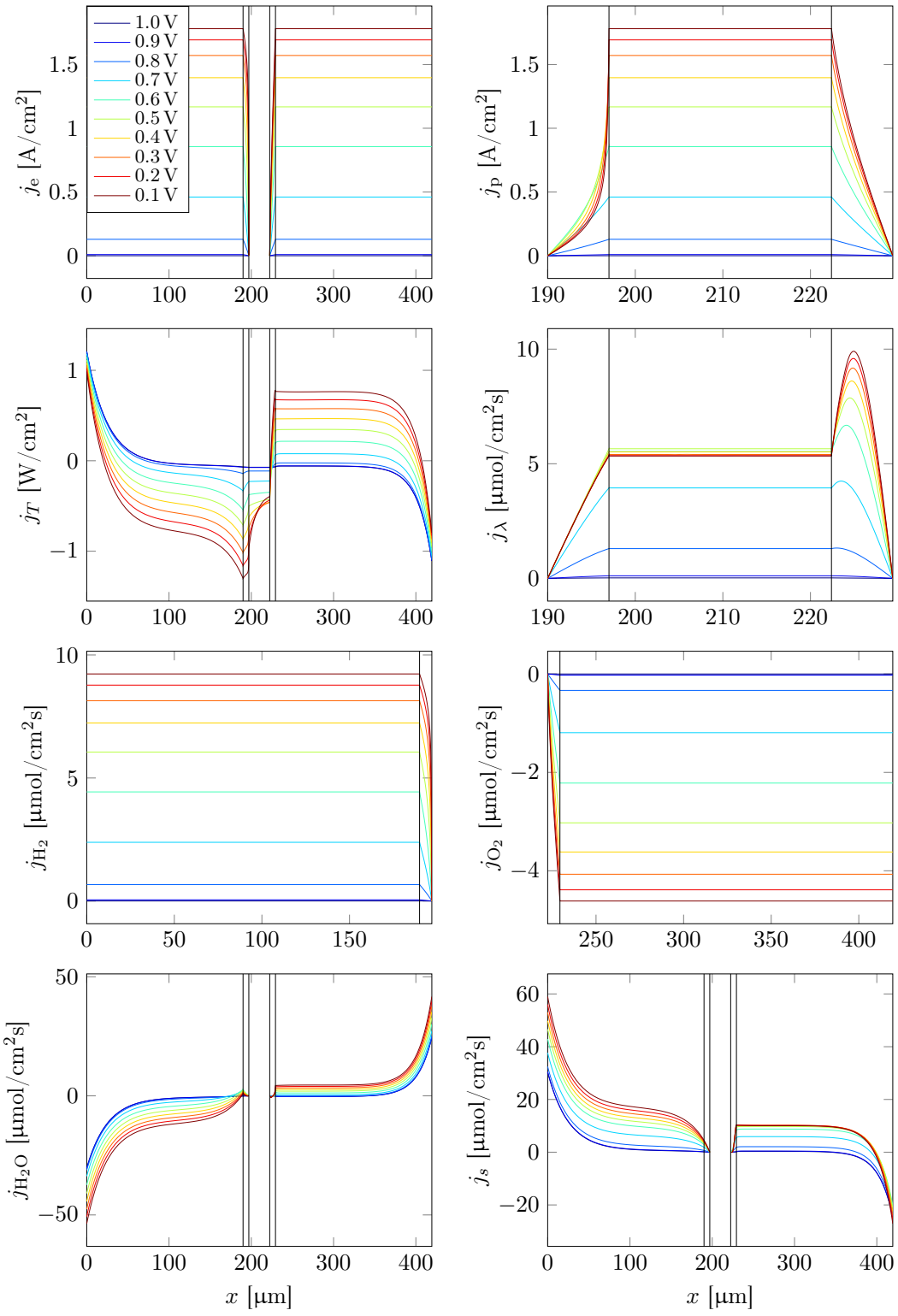

Figure 29: Fluxes through the membrane electrode assembly. j_e: electron current density; j_p: proton current density; j_T: thermal flux; j_λ: flux of dissolved water in the polymer electrolyte; j_{H2}: flux of hydrogen; j_{O2}: flux of oxygen; j_{H2O}: water vapor flux; j_s: flux of liquid water.

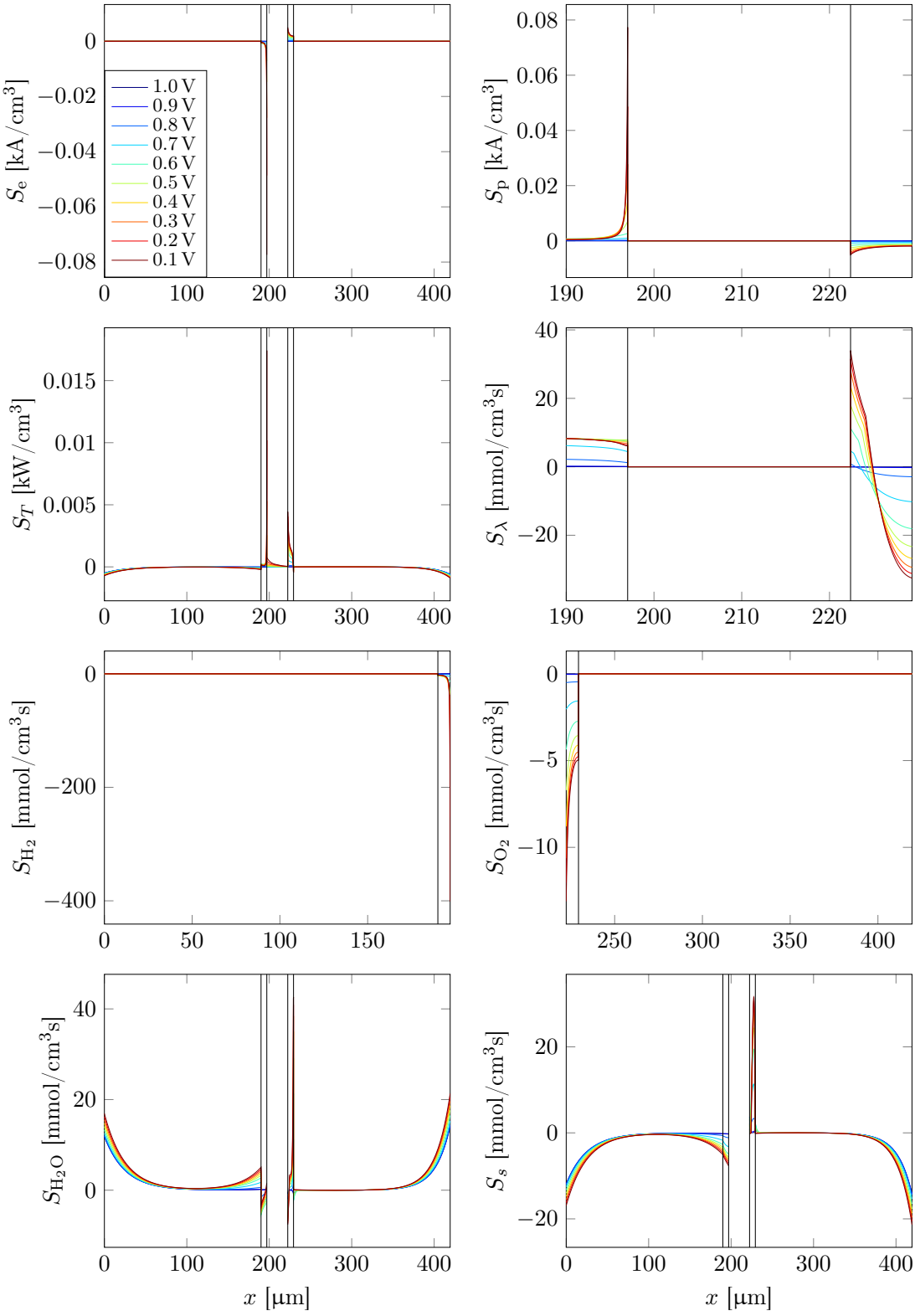

Figure 30: Local distribution of source terms of the continuity equations. S_e: electron source/sink; S_p: proton source/sink; S_T: heat source/sink; S_λ: source/sink of dissolved water in the polymer electrolyte; S_{H2}: sink of hydrogen; S_{O2}: sink of oxygen; S_{H2O}: source/sink of water vapor; S_s: source/sink of liquid water.

3.7. Master 1D MEA model (MMM)

The above-described fully-parameterized 1D model of an electrode assembly model of a PEFC has been re-implemented in a compact and well-documented form. The program code has been designed for:

- Simplicity and compactness. The code does not require manual differentiation of th equations. This dramatically simplifies modifications such as the substitution of individual parameterizations or boundary conditions, which can be done by replacing a single line of code. No lookup tables or data interpolation are involved.
- Portability and compatibility. The model is implemented as a standalone MATLAB function, relying only on MATLAB's standard boundary value problem solver. This choice ofcprogramming environment lets the simulation run on a large variety of platforms and also lets it benefit from MATLAB's widespread availability in science and industry.
- Transparency. The model equations and boundary conditions are fully disclosed, and the complete simulation output is published, including all potentials, fluxes and the entire polarization curve.
- Accessibility. The program is well documented and ready to be used out of the box. Modifying the code requires only minimal programming knowledge, running it requires none at all. All plots are automatically generated.
- Free availability. Our implementation is open-source and published under a BSD-like license permitting also commercial use. It thus provides a starting point for PEFC model building in industry and research, and a sound basis for modeling extensions such as time dependence, multi-dimensionality, or advanced material parameterizations.
- Establishment of a reference simulation. The model uses established and accepted parameterizations of steady-state through-plane transport processes. The MMM establishes a new basis for model comparison, benchmarking and validation.

At the time of writing the authors of this report are going to submit a manuscript to a peer-reviewed scientific journal to publish the MMM. We think it is important to establish an open reference implementation of a simple yet capable PEFC model to boost the use of modeling in fuel cell R&D, and to standardize model development in both academia and industry.
The MMM will be used to foster collaborations to develop material- and company-specific versions of the MMM that we name parameterized MEA models (PMM).

3.8. Fully parameterized 3D PEMFC model

A new cooperation between a French research group at DRT/Liten (liten.cea.fr) in Grenoble was initiated with the goal to compare 3D tomographic data of the water distribution in a small area test fuel cell to simulation results. This comparison between simulation results and the spatial water distribution at different operating conditions of the fuel cell will help to answer open questions regarding the transport and accumulation of liquid water in the porous layers and in the gas distribution channels. For example, the boundary conditions for the continuity equation for liquid water between the porous GDLs and the gas channel needs to match the experimental conditions. Moreover, phase change induced flow of water and the parameterization of the evaporation and condensation rates in the mathematical model can be critical to obtain realistic simulation results that enable the model-based design the porous layers.

An example geometry of the full 3D simulation is depicted in Figure 31. The MEA is represented as a sandwich of layers analogous to the 1D model. On each side, a fully parameterized single rectangular serpentine flow channel is added.

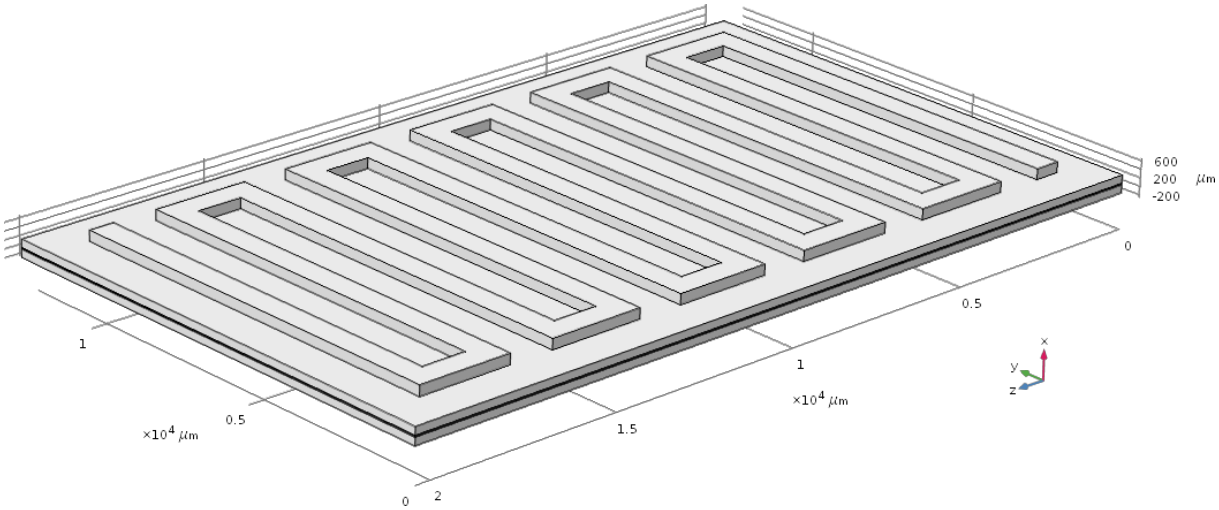

Figure 31: Three-dimensional setup of the small-area fuel cell with the MEA sandwich in the middle and a single rectangular serpentine flow channel on each side. An example with Nt = 10 turns is shown. The script to generate the channel geometry has been written to reproduce the geometry of test cells at DRT/Liten in Grenoble, France.

In order to realistically include the effect of gas flow in the flow channels and porous media, the assumption of uniform pressure made in the 1D MEA model described in Section 3.1 is relaxed for the present full 3D fuel cell model. Gas flow is assumed to be laminar and driven by convection and multicomponent diffusion. Flow conditions at the interface of an open flow field (gas channels) and a porous medium (gas diffusion layers) are difficult to model. Here, a manual implementation of the Stefan-Maxwell equations for gas species inter-diffusion are replaced by the “Transport of Concentrated Species” physics interface of Comsol Multiphysics with convection enabled. This solves a particular form of the convection-diffusion equation that includes the gradient of the total gas pressure P and a flow field velocity vector u. These are the dependent variables of the “Laminar Flow” physics interface, which solves for the pressure and velocity of the gas mixture assuming.
Currently, the model is being parameterized to match the material properties of test cells of the lab at Liten in Grenoble. Additionally, test simulations are being performed using different discretization meshes to enable convergence of the numerical solution algorithm for all experimentally chosen cell potentials.

4. National cooperation

The Institute of Computational Physics is in contact with the Swiss company Sefar AG to apply the project results. Sefar AG is developing and selling “smart fabrics” – these fabrics often consist of a polymer fabric as a basis with woven-in electrically conductive filaments and may serve for application in electrochemical cells, and particularly in fuel cells. Our aim is to perform a 3D analysis at the pore scale to the microstructures of different fabrics and then extract macro-homogeneous transport properties to simulate the corresponding fuel cell (or battery) performances. In combination with stochastic simulations these methods represent a powerful framework for virtual materials design, which shall lead to improvements of the materials properties and of the corresponding cell performance.

5. International cooperation

Several international cooperations based on the project results were continued and started in the year 2017:

- The ICP managed to continue an industry project (also in 2017) on fuel cell modeling with a large automotive company in Germany.
- The ICP is part of a new international consortium named ACTIF that aims at optimized operation strategies for automotive fuel cell systems regarding the three main aspects efficiency, life-time and costs on the stack level. The aim of the contribution of ICP to the consortium is to extend the 1D membrane electrode assembly modeling to time-dependent versions that serve to analyze the transient behavior of fuel cell stacks. The project is a French-German-Swiss initiative for research collaboration on fuel cells and hydrogen for automotive application. The Swiss/French company GreenGT will be part of the ACTIF consortium.
- A new cooperation between a French research group at DRT/Liten (liten.cea.fr) in Grenoble was initiated with the goal to compare the 3D stationary non-isothermal two-phase fuel cell model to tomographic data of the water distribution in a small area test fuel cell.
- A new cooperation between the ICP and the German Robert Bosch GmbH, Applied Research 1 - Chemical Processes and Technology - Energy Storage and Conversion (CR/ARC1) has been started. A master student of Bosch is working on the simulation of membrane electrode assemblies for PEFCs using the MMM program code developed in WP4.
- The project results have been successfully presented at the ModVal14 symposium on modelling and experimental validation of batteries and fuel cells in 2017. Moreover, the project results have been presented at the 7th International Conference on Fundamentals and Development of Fuel Cells, Stuttgart, January 2017.

6. Project evaluation and outlook

The methods for micro-macro relationships proposed in this project provide detailed and novel information and it is a new alternative to simple curve fitting, in the sense that complex patterns of anisotropy can be explained in terms of the dominant microstructure characteristics such as effective volume fraction, pore and bottleneck sizes, constrictivity, tortuosity or hydraulic radius. These methods are also suitable for investigations of wet GDL based on in-situ injection experiments with X-ray tomography. In comparison to conventional functions describing relative liquid permeability (e.g. Van-Genuchten, Brooks-Corey etc.) our investigations reveal more complex permeability-saturation curves (S-shaped), and this complexity can be explained based on the detailed microstructure information available through the mentioned 3D methods. Hence, these methods shed new light on the microstructure effects, which control the effective, macroscopic material properties.
The information on GDL properties gained so far at the pore-scale level will be used as input for macro-homogenous modelling at cell and stack levels, in order to link microstructure characteristics with cell performance. On a longer term the 3D analysis at pore scale shall be applied to a wide range of microstructures and then combined systematically with macro-homogeneous models that provide the corresponding cell performances. In combination with stochastic simulations these methods represent a powerful framework for virtual materials design, which shall lead to improvements of the materials properties and of the corresponding cell performance.

We successfully developed a set of macrohomogeneous models to simulate membrane electrode assemblies and small area PEFCs. The material parameterizations of these models were revised and updated to reflect the state-of-the art knowledge, and we are currently comparing simulation results to measurement data of different labs and companies. Transport properties extracted from tomographic images of the porous layers (e.g. electrical conductivity, permeability, diffusivity) can be extracted and used to simulate the fluxes of mass, charge and heat with the macrohomogeneous models. This is the key to predict the influence of multifunctional material design on the fuel cell performance. The methodology is highly interesting for companies in the value added chain of hydrogen fueled electric vehicles, other PEFC powered electric devices but also for other electrochemical cells.
For example, from 2018 on the ICP will take part in the European project FlowCamp. The goal of the FlowCamp project is to develop porous materials and macrohomogeneous models for three next generation redox-flow batteries (hydrogen-bromine, organic and zinc-air systems). Batteries will be constructed and systems will be upscaled to prototype level (TRL4/5), and validated using the cutting-edge battery testing facilities available for the RedoxWind project at the German Fraunhofer Institute for Chemical Technologies.
Moreover, we are in contact with Swiss and international companies for knowledge transfer of model based material design and PEFC analysis to the industry (see Sections 4 and 5). The web page www.isomorph.ch is being created for the marketing of mathematical models of electrochemical cells, offering consulting to companies and laboratories, and to disseminate selected project results.

7. Financial Report

PSI-LEC	Personnel category	Personnel: hourly rate SFOE [CHF/h]	Project hours financed by SFOE	Project Y1-Y3 SNSF	SFOE	OC	PSI-LEC Total [CHF]
Adrien Lamibrac	PostDoc		0	195'490	0	0	195'490
Technician	Technician			0	0	40'000	40'000
Travel costs				0	2'000	2'000	4'000
Materials, supplies, other costs				0	18'000	10'000	28'000
Total				195'490	20'000	52'000	267'490

ZHAW-ICP				Project Y1-Y3 SNSF	SFOE	OC	ZHAW-ICP Total [CHF]
Dujc	Research staff	60	360	12'515	21'600	4'525	38'640
Capone	Sci. assistant	50	182	39'315	9'100	20'635	69'050
Marmet	Research staff	60	586	25'409	35'160	7'891	68'460
Vetter	Research staff	60	0	54'321	0	4'745	59'066
Stenzel	Research staff	60	258	7'778	0	3'202	10'980
Holzer	Research staff	80	993	7'112	79'440	22'748	109'300
Pecho	Research staff	60	0	0	0	60'760	60'760
Sartoris	Research staff	60	447	0	26'820	21'380	48'200
Schumacher	Project leader	80	236	0	18'880	26'616	45'496
Travel costs, materials, supplies, other				0	0	42'885	42'885
Total			3062	146'450	191'000	215'387	552'837

PSI and ZHAW	Project Y1-Y3 SNSF	SFOE	OC	PSI and ZHAW Total [CHF]
Salaries personnel	341'998	191'000	212'502	745'500
Travel costs, materials, supplies, other	0	20'000	52'885	72'885
Total	341'998	211'000	265'387	818'385

8. References

8.1. Peer-reviewed publications in 2017

- [Holzer 2017a] L. Holzer, O. M Pecho, J.O. Schumacher, P. Marmet, O. Stenzel, F. N Büchi, A. Lamibrac, B. Münch: Microstructure-property relationships in a gas diffusion layer (GDL) for Polymer Electrolyte Fuel Cells, Part I: effect of compression and anisotropy of dry GDL, Electrochimica Acta, 227, p. 419-434, 2017. https://doi.org/10.1016/j.electacta.2017.01.030
- [Capone 2017] L. Capone, P. Marmet, A. Lamibrac, F.N. Büchi, L. Holzer, J. Dujc, J.O. Schumacher: *An ensemble Monte Carlo simulation study of water distribution in porous gas diffusion layers for proton exchange membrane fuel cells*, accepted for publication in the ASME Journal of Electrochemical Energy Conversion and Storage, 2017.
- [Dujc 2017] J. Dujc, P. Marmet, J.O. Schumacher, A. Forner-Cuenca, M. Cochet, P. Boillat: *Modelling the Effects of using Gas Diffusion Layers with Patterned Wettability for Advanced Water Management in Proton Exchange Membrane Fuel Cells.* Journal of Electrochemical Energy Conversion and Storage, 2017. DOI: 10.1115/1.4038626
- [Holzer 2017b] L. Holzer, O. Pecho, J.O. Schumacher, P. Marmet, F.N. Büchi, A. Lamibrac, B. Münch: *Microstructure-property relationships in a gas diffusion layer (GDL) for Polymer Electrolyte Fuel Cells, Part II: pressure-induced water injection and liquid permeability*, Electrochimica Acta, 241, p. 414-432, 2017. https://doi.org/10.1016/j.electacta.2017.04.141
- [Vetter] R. Vetter, J.O. Schumacher: *Free open reference implementation of a two-phase PEM fuel cell model*, manuscript to be submitted to the scientific journal Computer Physics Communications.

8.2. References to the open literature

[1] Packard, N. H., and S. Wolfram. "Two-dimensional cellular automata." *Journal of Statistical Physics* 38.5-6 (1985): 901-946.
[2] Allen, M. P., and D. J. Tildesley. *Computer simulation of liquids*. Oxford university press, 1989.
[3] Chib, S., and E. Greenberg. "Understanding the metropolis-hastings algorithm." *The american statistician* 49.4 (1995): 327-335.
[4] Billera, L. J., and P. Diaconis. "A geometric interpretation of the Metropolis-Hastings algorithm." *Statistical Science* (2001): 335-339.
[5] Landau, D. P., and K. Binder. *A guide to Monte Carlo simulations in statistical physics*. Cambridge university press, 2014.
[6] Huang, K. *Introduction to statistical physics*. CRC Press, 2009.
[7] Liu, J. S. *Monte Carlo strategies in scientific computing*. Springer Science & Business Media, 2008.
[8] Adamson, A. W., and Alice Petry Gast. "Physical chemistry of surfaces." (1997): 400-408.
[9] Cassie, A. B. D., and S. Baxter. "Wettability of porous surfaces." *Transactions of the Faraday Society* 40 (1944): 546-551.
[10] Wenzel, R. N. "Surface Roughness and Contact Angle." *The Journal of Physical Chemistry* 53.9 (1949): 1466-1467.
[11] De Gennes, P.-G. "Wetting: statics and dynamics." *Reviews of modern physics* 57.3 (1985): 827.
[12] Seidenberger, K., et al. "Estimation of water distribution and degradation mechanisms in polymer electrolyte membrane fuel cell gas diffusion layers using a 3D Monte Carlo model." *Journal of Power Sources* 196.12 (2011): 5317-5324.
[13] Kawasaki, K. "Kinetics of Ising models." *Phase transitions and critical phenomena* 2 (1972): 443-501.
[14] Berg, B. A., and A. Billoire. *Markov Chain Monte Carlo Simulations*. John Wiley & Sons, Inc., 2008.

[15] Wiegmann, A., S. Rief, and A. Latz. "Virtual material design and air filtration simulation techniques inside GeoDict and FilterDict." *AFS annual meeting, Atlanta*. 2005.
[16] Chatterjee, J. "Prediction of coupled menisci shapes by Young–Laplace equation and the resultant variability in capillary retention." *Journal of colloid and interface science* 314.1 (2007): 199-206.
[17] Lu, N., et al. "A Monte Carlo paradigm for capillarity in porous media." *Geophysical Research Letters* 37.23 (2010).
[18] Stenzel, O., M. Neumann, O. Pecho, V. Schmidt, L. Holzer, Predicting Effective Conductivities Based on Geometric Microstructure Characteristics, American Institute of Chemical Engineers (AIChE) Journal, submitted (2015).
[19] Holzer, L., O. Stenzel, O. Pecho, T. Ott, G. Boiger, M. Gorbar, et al., Fundamental relationships between 3D pore topology, electrolyte conduction and flow properties: Towards knowledge-based design of ceramic diaphragms for sensor applications, Material & Design, submitted (2015).

Contents

List of abbreviations

1D	One-dimensional
3D	Three-dimensional
CFD	Computational fluid dynamics
CH	Gas channel
CL	Catalyst layer
CT	Computed tomography
FIB-SEM	Focused ion beam scanning electron microscope
GDL	Gas diffusion layer
ICP	Institute of Computational Physics
IP	In-plane
MC	Monte Carlo
MEA	Membrane electrode assembly
MIP	Mercury intrusion porosimetry
MMM	Master MEA model
MPL	Micro-porous layer
PEFC	Polymer electrolyte fuel cell
PMM	Parameterized MEA model
PSD	Pore size distribution
PSI	Paul Scherrer Institute
PTFE	Polytetrafluoroethylene
TP	Through-plane
WPX	Work package X
ZHAW	Zurich University of Applied Sciences